The Astrophysical Journal, 934:110 (19pp), 2022 August 1 https://doi.org/10.3847/1538-4357/ac7aac

Spectroscopic Study of Four Metal-poor Carbon Stars from the Hamburg/ESO Survey: On Confirming the Low-mass Nature of Their Companions*

J. Shejeelammal and Aruna Goswami
Indian Institute of Astrophysics, Koramangala, Bangalore 560034, India; aruna@iiap.res.in
Received 2022 April 28; revised 2022 June 17; accepted 2022 June 17; published 2022 July 29

Abstract

Elemental abundances of extrinsic carbon stars provide insight into the poorly understood origin and evolution of elements in the early Galaxy. In this work, we present the results of a detailed spectroscopic analysis of four potential carbon star candidates from the Hamburg/ESO Survey (HES): HE 0457−1805, HE 0920−0506, HE 1241−0337, and HE 1327−2116. This analysis is based on the high-resolution spectra obtained with Mercator/HERMES ($R \sim 86{,}000$) and SUBARU/HDS ($R \sim 50{,}000$). Although the abundances of a few elements, such as Fe, C, and O, are available from medium-resolution spectra, we present the first ever detailed high-resolution spectroscopic analysis for these objects. The objects HE 0457−1805 and HE 1241−0337 are found to be CEMP-s stars, HE 0920−0506 a CH star, and HE 1327−2116 a CEMP-r/s star. The object HE 0457−1805 is a confirmed binary, whereas the binary status of the other objects is unknown. The locations of program stars on the diagram of absolute carbon abundance A(C) versus [Fe/H] point at their binary nature. We have examined various elemental abundance ratios of the program stars and confirmed the low-mass nature of their former AGB companions. We have shown that the i-process models could successfully reproduce the observed abundance pattern in HE 1327−2116. The analysis performed for HE 0457−1805, HE 0920−0506, and HE 1241−0337 based on the FRUITY parametric models confirmed that the surface chemical compositions of these three objects are influenced by pollution from low-mass AGB companions.

Unified Astronomy Thesaurus concepts: Chemical abundances (224); Chemically peculiar stars (226); Carbon stars (199)

Supporting material: machine-readable tables

1. Introduction

Low- and intermediate-mass stars (0.8–10 $M_{\odot}$) are the predominant stellar population of our Galaxy (Karakas & Lattanzio 2014). These stars are the main sites of various types of nucleosynthesis and important participants in the chemical evolution of the universe (Travaglio et al. 2001, 2004; Romano et al. 2010; Kobayashi et al. 2011, 2020). As they evolve through different stages of stellar evolution, they enrich the interstellar medium (ISM) through stellar outflows or winds. The pollution from these low- and intermediate-mass stars accounts for about 90% of the ISM dust, and massive stars account for the rest (Sloan et al. 2008). The majority of the elements heavier than Fe are produced by these stars through slow (s) and rapid (r) neutron-capture processes. The origin and evolution of these heavy elements still remain poorly understood. This underscores the need for detailed studies on different classes of stars enhanced in heavy elements, for instance Ba, CH, carbon-enhanced metal-poor (CEMP) stars etc. The last two decades have witnessed a significant increase in high-resolution spectroscopic studies of these groups of stars.

Ba and CH stars show enhanced abundances of s-process elements. CEMP stars are metal-poor counterparts ([Fe/H] < -1) of CH stars (e.g., Lucatello et al. 2005; Abate et al. 2016). A fraction of them show enrichment of s- and/or r-process elements. They are classified into four subclasses: CEMP-r (enhanced in r-process elements), CEMP-s (enhanced in s-process elements), CEMP-r/s (enhanced in both s- and r-process elements), and CEMP-no (little or no enhancement of heavy elements) (Beers & Christlieb 2005). The suggested origin for CEMP-r stars is that they were formed from the ISM pre-enriched by events, such as core-collapse supernovae (SNe), neutron star mergers, and neutron star—black hole mergers (Surman et al. 2008; Arcones & Thielemann 2013; Rosswog et al. 2014; Drout et al. 2017; Lippuner et al. 2017). The suggested progenitors for the origin of carbon enhancement of CEMP-no stars, which polluted the ISM, are faint SNe, spinstars, metal-free massive stars, and binary mass transfer from extremely metal-poor asymptotic giant branch (AGB) stars (Heger & Woosley 2010; Nomoto et al. 2013; Chiappini 2013; Tominaga et al. 2014).

CEMP-s stars are metal-poor analogs of CH and Ba stars, and binary mass transfer from former AGB companion stars has been identified as the source of their observed abundance pattern (e.g., Jorissen et al. 1998, 2016a; Lucatello et al. 2005; Starkenburg et al. 2014; Hansen et al. 2016b). However, the exact origin of CEMP-r/s stars is an open question (Jonsell et al. 2006; Masseron et al. 2010; Koch et al. 2019). Studies have shown that almost half of CEMP-s stars are CEMP-r/s stars (Sneden et al. 2008; Käppeler et al. 2011; Bisterzo et al. 2011). Just like the CEMP-s stars, CEMP-r/s stars are also found to belong to binary systems (Lucatello et al. 2005; Starkenburg et al. 2014; Hansen et al. 2016b). The scenarios proposed to explain the origin of CEMP-r/s stars include: self-pollution of a star formed from r-element-enriched ISM,

* Based on data collected using Mercator/HERMES, SUBARU/HDS.

Table 1
Basic Information on the Program Stars

Star	R.A.(2000)	Decl.(2000)	*B*	*V*	*J*	*H*	*K*	S/N 4200 Å	S/N 5500 Å	S/N 7700 Å
HE 0457−1805	04 59 43.56	−18 01 11.99	12.372	11.014	8.937	8.421	8.186	15.82	55.48	89.05
HE 0920−0506	09 23 05.96	−05 19 32.75	11.80	10.95	10.317	9.971	9.900	14.00	51.88	49.89
HE 1241−0337	12 44 27.21	−03 54 01.20	15.84	14.30	11.869	11.234	11.026	8.35	40.16	⋯
HE 1327−2116	13 30 19.36	−21 32 03.33	12.714	11.651	9.893	9.412	9.275	13.85	29.60	68.14

pollution from an AGB companion in a binary system formed from r-element-enriched ISM, a binary system polluted from the massive primary in a tertiary system, and a secondary star polluted from the primary exploded as a Type 1.5 SN or intermediate neutron-capture (i) process (Jonsell et al. 2006 and references therein, Hampel et al. 2016). The i-process, originally proposed by Cowan & Rose (1977), produces neutron density intermediate between s- and r-processes, of the order of 10^{15-17} cm^{-3}. There are a number of sites proposed to host the i-process, such as rapidly accreting white dwarfs (Denissenkov et al. 2017), super-AGB stars of low metallicity (Doherty et al. 2015; Jones et al. 2016), metal-poor massive ($M \geqslant 20\ M_{\odot}$) stars (Banerjee et al. 2018), extremely low-metallicity ($z \leqslant 10^{-5}$) low-mass AGB stars (Fujimoto et al. 1990; Hollowell et al. 1990; Lugaro et al. 2009), low-mass ($M \leqslant 2\ M_{\odot}$) very low-metallicity ($z \leqslant 10^{-4}$) AGB stars (Fujimoto et al. 2000; Campbell & Lattanzio 2008; Lau et al. 2009; Cristallo et al. 2009; Campbell et al. 2010; Stancliffe et al. 2011). etc., though the exact site(s) is not confirmed yet. Several studies used the i-process in low-mass low-metallicity AGB stars to successfully explain the abundances of CEMP-r/s stars (Hampel et al. 2016; Karinkuzhi et al. 2021; Goswami et al. 2021; Shejeelammal et al. 2021; Shejeelammal & Goswami 2021; Purandardas & Goswami 2021).

In this work, we present the results of a detailed high-resolution spectroscopic analysis of four carbon stars identified from the Hamburg/ESO Survey (HES). The structure of the paper is as follows. The stellar sample, source of the spectra, and data reduction are discussed in Section 2. Section 3 provides a discussion on radial velocity. Estimation of stellar atmospheric parameters, along with the discussion on stellar mass, is provided in Section 4. We discuss abundance determination in Section 5 and abundance uncertainties in Section 6. Classification of program stars is presented in Section 7. A detailed discussion on various abundance ratios of the program stars is provided in Section 8. A discussion on the origin of the program stars, along with the parametric model-based analysis, is also given in the same section. This section also contains a discussion on individual stars. Conclusions are drawn in Section 9.

2. Stellar Sample: Selection, Observation/Data Acquisition, and Data Reduction

All the four objects analyzed in this study—HE 0457−1805, HE 0920−0506, HE 1241−0337, and HE 1327−2116—are selected from the candidate metal-poor stars identified from the HES (Christlieb 2003). The stars HE 0457−1805 and HE 1241−0337 are listed in the catalog of carbon stars identified from the HES by Christlieb et al. (2001). The object HE 0457−1805 is also listed as a potential CH star candidate by Goswami (2005). The objects HE 0920−0506 and HE 1327−2116 are listed in the catalog of bright metal-poor candidates from the HES by Frebel et al. (2006). The wavelength-calibrated, high-resolution ($R \sim 50{,}000$) spectrum of HE 1241−0337 is taken from the SUBARU/HDS archive (http://jvo.nao.ac.jp/portal/v2/). The wavelength coverage of this spectrum is 4100–6850 Å with a wavelength gap between 5440 and 5520 Å. The high-resolution ($R \sim 86{,}000$) spectra of the objects HE 0457−1805, HE 0920−0506, and HE 1327−2116 were obtained using the High-Efficiency and High-Resolution Mercator Echelle Spectrograph (HERMES) attached to the 1.2 m Mercator telescope at the Roque de los Muchachos Observatory in La Palma, Canary Islands, Spain, operated by the Institute of Astronomy of the KU Leuven, Belgium (Raskin et al. 2011). The data were reduced using the HERMES pipeline. The HERMES spectra cover the wavelength range 3770–9000 Å. Multiple frames of each object were taken on different nights: 15 frames with exposures of 1800 and 2100 s for HE 0457−1805 during the period 2013–2016, 10 frames with exposures ranging from 750 to 1800 s for HE 0910−0506 during 2018–2020, and three frames with exposures of 1200 s for HE 1327−2116 on 2019 January 31 and 2019 February 1. To maximize the signal-to-noise ratio (S/N), all these frames were coadded after the Doppler correction. The coadded spectra are then continuum-fitted for further analysis, using IRAF[1] software. Table 1 provides basic information about the program stars, and the sample spectra are shown in Figure 1.

3. Radial Velocity

The radial velocities of the program stars are estimated from the measured shift in wavelength of several spectral lines using the Doppler equation. Then, the obtained radial velocity is corrected for heliocentric motion. The average value of these corrected velocities is taken as the radial velocity of the object. The detailed radial velocity data of the objects analyzed in this study are to be published in a summary paper on orbits of CEMP stars (Jorissen et al., in preparation). The estimated radial velocities, along with the values from the Gaia DR2 (Gaia Collaboration et al. 2018) and RAVE DR4 (Kordopatis et al. 2013), are given in Table 2. The object HE 0457−1805 is a confirmed binary with an orbital period of 2724 ± 23 days (Jorissen et al. 2016a). Our estimate of the radial velocity of this object differs from the Gaia value by $\sim$2 km s^{-1} and from the RAVE value by $\sim$9 km s^{-1}. For the object HE 0920−0506, our estimate shows a difference of $\sim$3 km s^{-1} from the Gaia value. This may indicate that this star is likely a binary. For the other object, HE 1327−2116, our estimates show a difference of $\sim$0.7 km s^{-1} from the Gaia and RAVE values. Estimates of radial velocity for the object HE 1241−0337 are not available in Gaia and RAVE.

[1] IRAF (Image Reduction and Analysis Facility) is distributed by the National Optical Astronomical Observatories, which is operated by the Association for Universities for Research in Astronomy, Inc., under contract to the National Science Foundation.

Table 2
Derived Atmospheric Parameters and Radial Velocity of the Program Stars

Star	$T_{\rm eff}$ (K) ±100	log g (cgs) ±0.2	ζ (km s^{-1}) ±0.2	[Fe I/H]	[Fe II/H]	V_r (km s^{-1}) This work	V_r (km s^{-1}) Gaia	V_r (km s^{-1}) RAVE	Reference
HE 0457−1805	4435	0.70	1.97	−1.98 ± 0.13	−1.98 ± 0.12	+62.83 ± 0.02	+60.80 ± 0.35	72.00 ± 2.2	1
	4484	0.77	⋯	−1.46	⋯	⋯	⋯	⋯	2
HE 0920−0506	5380	2.65	0.69	−0.75 ± 0.06	−0.75 ± 0.01	+49.60 ± 0.03	+52.44 ± 1.27	⋯	1
	⋯	⋯	⋯	−1.01	⋯	⋯	⋯	⋯	3
	5291	2.99	⋯	−1.39	⋯	⋯	⋯	⋯	4
HE 1241−0337	4240	1.18	2.82	−2.47 ± 0.13	−2.47 ± 0.09	+179.69 ± 2.18	⋯	⋯	1
HE 1327−2116	4835	1.50	3.45	−2.84 ± 0.07	−2.84 ± 0.05	+176.77 ± 0.06	+177.43 ± 1.46	177.4 ± 1.5	1
	⋯	⋯	⋯	−2.93	⋯	⋯	⋯	⋯	3
	4868	0.55	⋯	−3.48	⋯	⋯	⋯	⋯	4

References: 1, Our work; 2, Kennedy et al. (2011); 3, Frebel et al. (2006); 4, Beers et al. (2017).

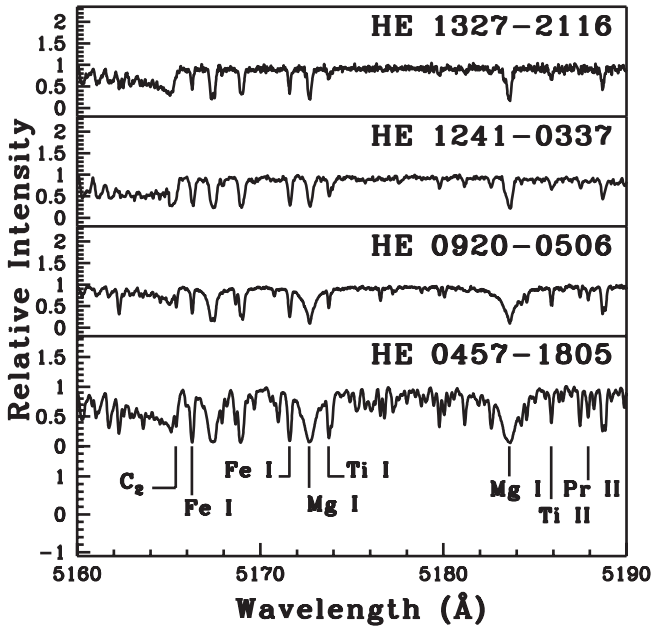

Figure 1. Sample spectra of the program stars in the wavelength region 5160–5190 Å.

4. Stellar Atmospheric Parameters

The stellar atmospheric parameters of the program stars are derived from the measured equivalent widths of the clean Fe I and Fe II lines with excitation potential and equivalent width, respectively, in the ranges 0–6.0 eV and 10–180 mÅ. The radiative transfer code MOOG (Sneden 1973) is used for our analysis under the assumption of local thermodynamic equilibrium (LTE). The model atmosphere is selected from the Kurucz grid of model atmospheres with no convective overshooting (Castelli & Kurucz 2003, http://kurucz.harvard.edu/grids.html). To select the initial model atmosphere to start with, we have used the estimates of photometric temperature calculated from the calibration equations given by Alonso et al. (1999, 2001) and a guess for a typical log g value for giants. Using the usual method of excitation balance and ionization balance, the final model atmosphere is obtained through an iterative process from the initial one. The detailed procedure is described in our earlier papers (Shejeelammal et al. 2020, 2021; Shejeelammal & Goswami 2021). Derived Fe abundances of the program stars are shown in Figure 2, and their derived atmospheric parameters are given in Table 2. The literature values of these atmospheric parameters are also provided in the same table. The comparison of our estimates of stellar atmospheric parameters with the literature values is discussed in Section 8.5.

The surface gravity is also calculated from the parallax method using

$$\log(g/g_{\odot}) = \log(\mathrm{M/M_{\odot}}) + 4\log(\mathrm{T_{eff}/T_{eff\odot}}) - \log(\mathrm{L/L_{\odot}}).$$

The adopted solar values are log $g_{\odot} = 4.44$, $T_{\rm eff\odot} = 5770$ K, and $M_{\rm bol\odot} = 4.74$ mag. The masses of the program stars are found from their positions on the H-R diagram (log $T_{\rm eff}$ versus log($L/L_{\odot}$)) generated using the evolutionary tracks of Girardi et al. (2000). This procedure is discussed in detail in Shejeelammal et al. (2020). $z = 0.0004$ ([Fe/H] ~ -1.7) tracks were used for the objects HE 0457−1805 and HE 1327−2116, and $z = 0.004$ ([Fe/H] ~ -0.7) tracks for HE 0920−0506. The positions of the program stars on the H-R diagram are shown in Figure 3. We could find only an upper limit to the mass of the star HE 0457−1805. We could not estimate the mass of the star HE 1241−0337 since its parallax value is not available. The estimated mass and log g values of the program stars are given in Table 3. For the star HE 0920−0506, the spectroscopic log g is ∼0.8 dex lower than that estimated from the parallax method. In some carbon stars, such an inconsistency between the spectroscopic atmospheric parameters and those derived from the evolutionary tracks could arise as their evolutionary tracks shift toward lower temperatures (Marigo 2002; Jorissen et al. 2016b). The spectroscopic log g values have been used for our analysis.

5. Abundance Determination

The elemental abundances were estimated with two methods: (i) using the equivalent widths of the spectral lines and (ii) by comparison of observed spectra and synthetic spectra generated with MOOG (spectral synthesis calculation), using Kurucz model atmospheres (http://kurucz.harvard.edu/grids.html). The spectral synthesis calculation is performed to derive the abundances of elements with hyperfine splitting (HFS) as well as for molecular bands. The hyperfine components of each atomic line, whenever available, are considered for the abundance estimation. In the case of abundance determination using the equivalent width method, the spectral line identification is performed by comparing the stellar spectra with the Doppler-corrected spectrum of Arcturus.

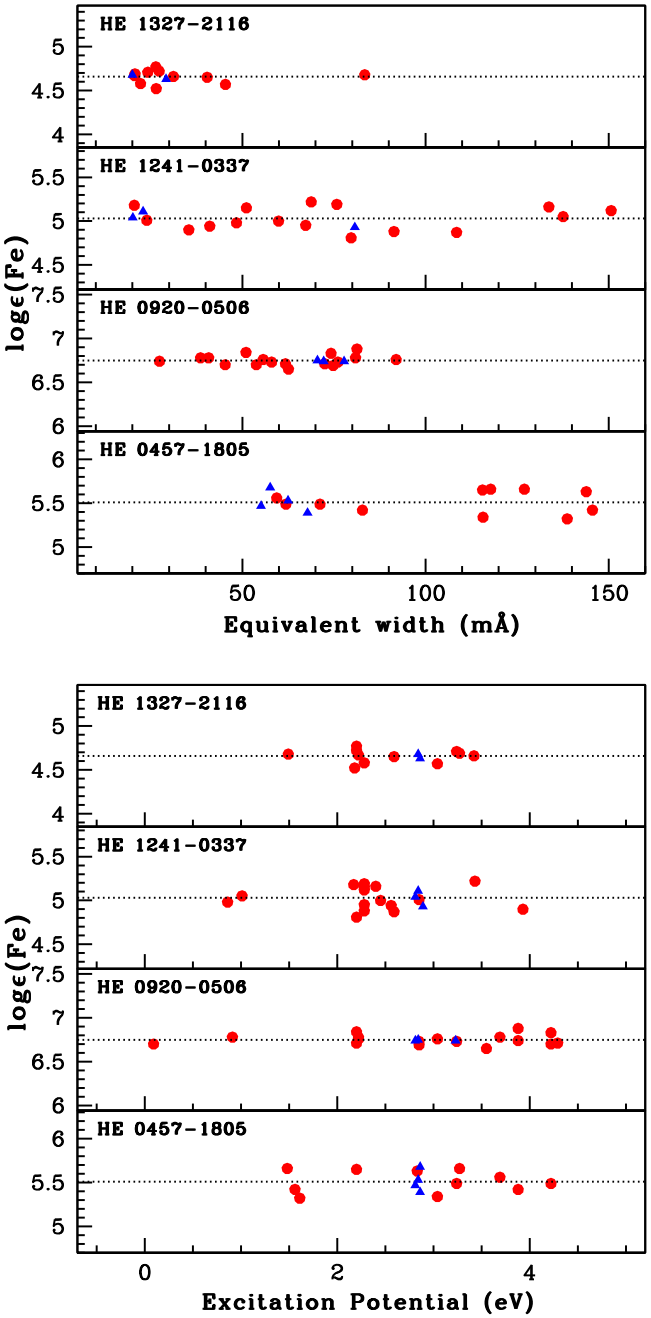

Figure 2. Fe abundances of the program stars derived from individual Fe I and Fe II lines as a function of equivalent width (upper panel) and excitation potential (lower panel). The adopted value of Fe abundance of each star is shown by the dotted lines. Solid circles and triangles represent Fe I and Fe II lines, respectively.

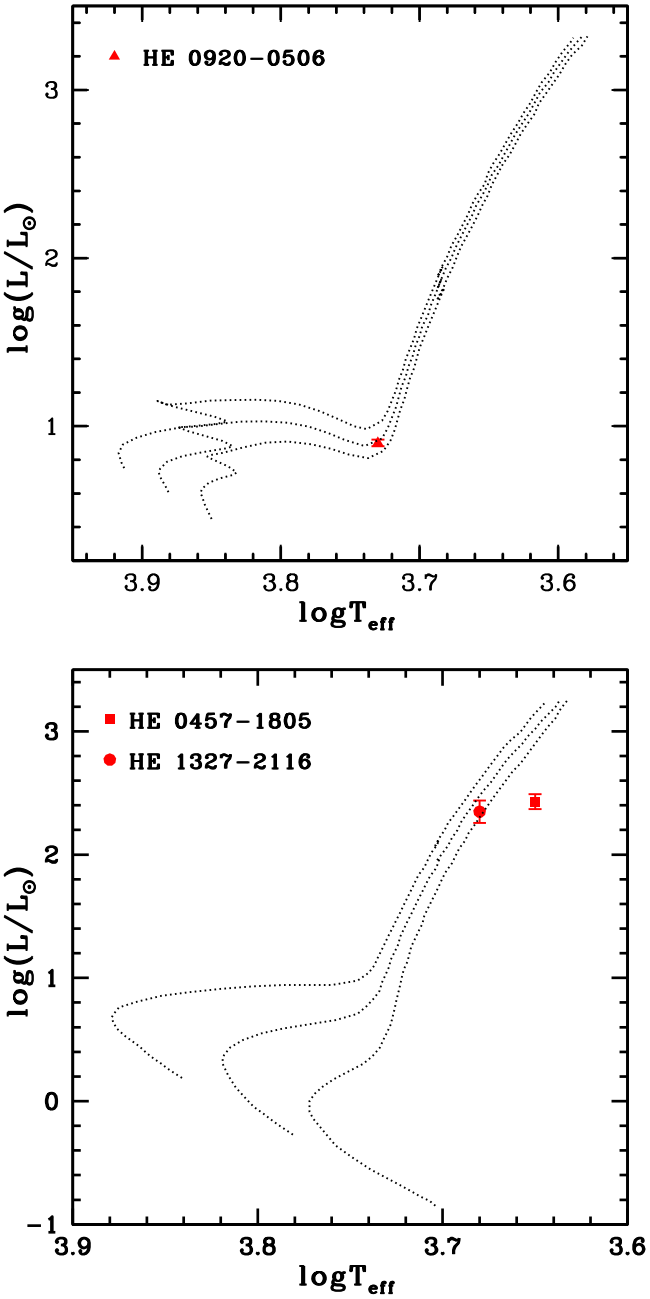

Figure 3. The evolutionary tracks for 1.0, 1.1, and 1.4 $M_{\odot}$ for $z = 0.004$ (upper panel) and for 0.6, 0.8, and 1.0 $M_{\odot}$ for $z = 0.0004$ (lower panel) are shown from bottom to top.

The line parameters are taken from the linemake[2] atomic and molecular line database (Placco et al. 2021).

Although the abundance estimation is performed under the assumption of LTE, we have applied the non-LTE (NLTE) corrections whenever available. The solar abundance values are adopted from Asplund et al. (2009). The details of the abundances of each element and the details of NLTE corrections as well as HFS are discussed in this section. The estimated elemental abundances in the program stars are given in Tables 4 and 5. The atomic lines used to derive the abundances of each elemental species are given in the Appendix in Tables A1–A3.

[2] linemake contains laboratory atomic data (transition probabilities, hyperfine and isotopic substructures) published by the Wisconsin Atomic Physics and the Old Dominion Molecular Physics groups. These lists and accompanying line list assembly software have been developed by C. Sneden and are curated by V. Placco at https://github.com/vmplacco/linemake.

5.1. Light Elements: C, N, O, $^{12}C/^{13}C$, Na, α-, and Fe-peak Elements

The oxygen abundance could be derived only in HE 0920 −0506, where we have used the spectral synthesis calculation of the [O I] line at 6300.304 Å. Oxygen is found to be slightly underabundant in this star with a value [O/Fe] ∼ −0.14. We could not detect a good [O I] 6300.304 Å line in other stars.

Table 3
Mass and log g Estimated from the Parallax Method

Star Name	Parallax (mas)	M_{bol}	$\log(L/L_{\odot})$	Mass ($M_{\odot}$)	log g (cgs)	log g (spectroscopic) (cgs)
HE 0457−1805	0.467 ± 0.0309	-1.341 ± 0.14	2.43 ± 0.05	<0.60	...	0.70
HE 0920−0506	2.3764 ± 0.0653	2.488 ± 0.06	0.90 ± 0.02	1.30 ± 0.005	3.50 ± 0.03	2.65
HE 1327−2116	0.3428 ± 0.0358	-1.130 ± 0.228	2.35 ± 0.09	0.70 ± 0.10	1.63 ± 0.03	1.50

Table 4
Elemental Abundances in HE 0457−1805 and HE 0920−0506

			HE 0457−1805				HE 0920−0506			
	Z	Solar log ϵ[a]	log ϵ	[X/H]	[X/Fe]	N	log ϵ	[X/H]	[X/Fe]	N
C[b] (C_2 band 5165 Å)	6	8.43	8.32	−0.11	1.87	...	8.20	−0.23	0.52	...
C[b] (C_2 band 5635 Å)	6	8.43	8.17	−0.26	1.72	...	8.30	−0.13	0.62	...
$^{12}C/^{13}C$[b]	...	...	...	...	23 ± 4	...	...	...	...	...
N[b]	7	7.83	7.52 ± 0.07	−0.31	1.67	3	7.53 ± 0.20	−0.30	0.45	3
O[b]	8	8.69	...	...	...	...	7.80	−0.89	−0.14	1
Na I	11	6.24	6.46 ± 0.06	0.22	2.2	3	5.94 ± 0.09	−0.30	0.45	3
Mg I	12	7.6	6.94 ± 0.14	−0.66	1.32	2	7.50 ± 0.03	−0.10	0.65	3
Si I	14	7.51	5.98 ± 0.17	−1.53	0.45	2	7.14 ± 0.17	−0.37	0.38	2
Ca I	20	6.34	5.21 ± 0.12	−1.13	0.85	7	5.98 ± 0.11	−0.36	0.39	16
Sc II[b]	21	3.15	1.85	−1.30	0.68	1	2.14	−1.09	−0.26	2
Ti I	22	4.95	3.83 ± 0.17	−1.12	0.86	6	4.40 ± 0.08	−0.55	0.2	8
Ti II	22	4.95	3.40 ± 0.14	−1.55	0.43	5	4.34 ± 0.08	−0.61	0.14	8
V I[b]	23	3.93	2.73	−1.20	0.78	2	2.87	−1.06	−0.31	1
Cr I	24	5.64	4.72 ± 0.10	−0.92	1.06	4	5.36 ± 0.09	−0.28	0.47	10
Cr II	24	5.64	4.58 ± 0.04	−1.06	0.92	2	5.37 ± 0.07	−0.27	0.48	3
Mn I[b]	25	5.43	4.43	−1.00	0.98	2	4.44 ± 0.01	−0.99	−0.24	2
Fe I	26	7.5	5.52 ± 0.13	−1.98	...	11	6.75 ± 0.06	−0.75	...	17
Fe II	26	7.5	5.52 ± 0.12	−1.98	...	4	6.75 ± 0.01	−0.75	...	3
Co I[b]	27	4.99	3.58	−1.41	0.57	1	4.19	−0.80	−0.05	1
Ni I	28	6.22	5.30 ± 0.08	−0.92	1.06	7	5.83 ± 0.10	−0.39	0.36	10
Cu I[b]	29	4.19	2.21	−1.98	0	1	3.19	−1.00	−0.25	1
Zn I	30	4.56	3.10	−1.50	0.48	1	4.34 ± 0.12	−0.22	0.53	2
Rb I[b]	37	2.52	1.95	−0.57	1.41	1	1.70	−0.82	−0.07	1
Sr I_{NLTE}[b]	38	2.87	2.54	−0.33	1.65	1	3.57	0.7	1.45	1
Y I[b]	39	2.21	3.01	0.8	2.78	1	2.32	0.11	0.86	1
Y II	39	2.21	2.18 ± 0.20	−0.03	1.95	4	2.67 ± 0.11	0.46	1.21	6
Zr I[b]	40	2.58	3.03	0.45	2.43	1	3.05	0.47	1.22	1
Zr II[b]	40	2.58	2.63	0.05	2.03	1	2.38	−0.20	0.55	1
Ba II_{LTE}[b]	56	2.18	...	...	...	...	2.83	0.65	1.4	1
Ba II_{NLTE}[b]	56	2.18	2.73	0.55	2.53	1	2.83	0.65	1.4	1
La II[b]	57	1.1	1.39 ± 0.02	0.29	2.27	3	1.60	0.5	1.25	2
Ce II	58	1.58	1.95 ± 0.15	0.37	2.35	6	1.99 ± 0.14	0.41	1.16	6
Pr II	59	0.72	1.30 ± 0.11	0.58	2.56	6	1.15 ± 0.03	0.43	1.18	2
Nd II	60	1.42	1.81 ± 0.11	0.39	2.37	9	1.74 ± 0.14	0.32	1.07	4
Sm II	62	2.41	1.39 ± 0.11	0.43	2.41	7	1.57 ± 0.18	0.61	1.36	4
Eu II_{LTE}[b]	63	0.52	−0.20	−0.72	1.26	1	−0.39	−0.91	−0.16	1
Eu II_{NLTE}[b]	63	0.52	...	...	...	...	−0.43	−0.95	−0.20	1

Notes.
[a] Asplund et al. (2009).
[b] Indicates that the abundances are derived from the spectral synthesis method. N is the number of lines used to derive the abundance. NLTE refers to the abundance derived from the lines affected by NLTE, after the corrections have been applied.

The [O I] line at 6363.776 Å and the oxygen triplet at 7770 Å were not usable for abundance determination in any of the program stars.

We could determine the carbon abundance in all the four program stars. The carbon abundance is derived from the spectral synthesis calculation of C_2 bands around 5165 and 5635 Å, except for HE 1241−0337 where the C_2 5165 Å band is noisy. The carbon abundances estimated from these two bands are consistent within 0.15 dex, and the final carbon abundance is taken to be the average of these two abundance values. While the star HE 0920−0506 shows a moderate enhancement of carbon with $[C/Fe] \sim 0.57$, the other three

Table 5
Elemental Abundances in HE 1241−0337 and HE 1327−2116

			HE 1241−0337				HE 1327−2116			
	Z	Solar log ϵ[a]	log ϵ	[X/H]	[X/Fe]	N	log ϵ	[X/H]	[X/Fe]	N
C[b] (C_2 band 5165 Å)	6	8.43	...	...	...	...	8.05	−0.38	2.46	...
C[b] (C_2 band 5635 Å)	6	8.43	8.53	0.10	2.57	...	8.05	−0.38	2.46	...
$^{12}C/^{13}C$[b]	...	...	...	...	...	...	...	...	7 ± 3	...
N[b]	7	7.83	6.38	−1.45	1.02	...	7.50 ± 0.10	−0.33	2.51	3
Na I	11	6.24	5.35 ± 0.18	−0.89	1.58	2	4.28	−1.96	0.88	1
Mg I	12	7.6	5.17 ± 0.13	−2.43	0.04	2	5.22	−2.38	0.46	1
Si I	14	7.51	5.82 ± 0.10	−1.69	0.78	2	5.45	−2.06	0.78	1
Ca I	20	6.34	4.15 ± 0.15	−2.19	0.28	6	4.13 ± 0.06	−2.21	0.63	5
Sc II[b]	21	3.15	1.00 ± 0.13	−2.15	0.32	2	0.03 ± 0.01	−3.12	−0.27	2
Ti I	22	4.95	2.77 ± 0.12	−2.18	0.29	3	2.77 ± 0.02	−2.18	0.66	2
Ti II	22	4.95	2.53 ± 0.19	−2.42	0.05	4	2.59 ± 0.08	−2.36	0.48	4
Cr I	24	5.64	...	...	...	...	3.03 ± 0.01	−2.61	0.23	2
Cr II	24	5.64	3.55 ± 0.03	−2.09	0.38	2	...	...	...	...
Mn I[†]	25	5.43	3.55	−1.88	0.59	1	3.61 ± 0.03	−1.81	1.03	2
Fe I	26	7.5	5.03 ± 0.13	−2.47	...	16	4.66 ± 0.07	−2.84	...	11
Fe II	26	7.5	5.03 ± 0.09	−2.47	...	3	4.66 ± 0.04	−2.84	...	2
Co I	27	4.99	...	...	...	...	1.81 ± 0.07	−3.18	−0.34	2
Ni I	28	6.22	3.64 ± 0.15	−2.58	−0.11	4	4.69 ± 0.06	−1.53	1.31	3
Zn I	30	4.56	1.81	−2.75	−0.28	1	2.16	−2.40	0.44	1
Sr I_{NLTE}[b]	38	2.87	1.54	−1.33	1.14	1	...	...	...	...
Y II	39	2.21	0.86 ± 0.11	−1.35	1.12	5	0.06 ± 0.02	−2.15	0.69	2
Zr I[†]	40	2.58	1.44	−1.14	1.33	1	1.81	−0.77	2.07	1
Zr II	40	2.58	1.54 ± 0.04	−1.04	1.43	4	0.89[b]	−1.69	1.15	1
Ba II_{NLTE}[b]	56	2.18	0.75	−1.43	1.04	1	1.08	−1.10	1.74	1
La II[b]	57	1.1	−0.35	−1.45	1.02	1	0	−1.10	1.74	1
Ce II	58	1.58	0.27 ± 0.19	−1.31	1.16	3	0.49 ± 0.10	−1.09	1.75	5
Pr II	59	0.72	-0.43 ± 0.12	−1.15	1.32	3	−0.23	−0.95	1.89	1
Nd II	60	1.42	-0.03 ± 0.12	−1.45	1.02	4	0.36 ± 0.08	−1.06	1.78	8
Sm II	62	2.41	-0.52 ± 0.01	−1.48	0.99	2	-0.07 ± 0.15	−1.03	1.81	4
Eu II_{LTE}[b]	63	0.52	-1.43 ± 0.15	−1.95	0.52	2	−1.16	−1.68	1.16	1

Notes.
[a] Asplund et al. (2009).
[b] Indicates that the abundances are derived from the spectral synthesis method. *N* is the number of lines used to derive the abundance. NLTE refers to the abundance derived from the lines affected by NLTE, after the corrections have been applied.

stars are enhanced in carbon with [C/Fe] > 1.70. The spectral synthesis fits of the two carbon bands in the program stars are shown in Figure 4.

We could estimate nitrogen in all the program stars. In HE 1241−0337, the nitrogen abundance is estimated from the spectrum synthesis of the ^{12}CN band at 4215 Å. In the other three program stars, nitrogen abundance is derived from the spectral synthesis calculation of ^{12}CN lines around 8000 Å. Among the program stars, the object HE 1327−2116 shows the highest enhancement of nitrogen with [N/Fe] ∼ 2.51.

The carbon isotopic ratio, $^{12}C/^{13}C$, is derived using the spectral synthesis calculation of ^{12}CN and ^{13}CN lines around 8000 Å. We could not estimate the value of the $^{12}C/^{13}C$ ratio in HE 0920−0506 because the ^{13}CN lines were not good, or in HE 1241−0337 because this region is not present in its spectrum. The values obtained for this ratio in the stars HE 0457−1805 and HE 1327−2116 are 23 ± 4 and 7 ± 3, respectively.

The abundances of elements Na, Mg, Si, Ca, Ti, Cr, Ni, and Zn are estimated from the measured equivalent widths of spectral lines listed in Table A2. We could estimate the abundances of all these elements in all the program stars. The object HE 0457−1805 shows the largest enhancement of Na with [Na/Fe] ∼ 2.20. While HE 1241−0337 and HE 1327−2116 show an enhancement of [Na/Fe] ∼ 1.58 and 0.88, respectively, Na is moderately enhanced in HE 0920−0506 with [Na/Fe] ∼ 0.45. In very metal-poor stars, Na suffers large uncertainties due to NLTE corrections or 3D hydrodynamical model atmospheres (Bisterzo et al. 2011; Andrievsky et al. 2007). The NLTE effect may reduce the Na abundance by up to ∼0.7 dex (Andrievsky et al. 2007). However, the Na I 5682.633, 5688.205, 6154.226, and 6160.747 Å lines have negligible NLTE effect (Takeda et al. 2003; Lind et al. 2011). We have used these weak lines to derive the Na abundance. The Mg abundance is derived mainly from Mg I 4702.991, 5528.405, and 5711.088 Å lines. The object HE 0457−1805 is enhanced in Mg as well with [Mg/Fe] ∼ 1.32. The object HE 1241−0337 shows a near-solar value, whereas the other two objects show moderate enhancement of Mg.

We have used the spectral synthesis calculation to derive the abundances of the elements Sc, V, Mn, Co, and Cu by incorporating their hyperfine components whenever available. The Sc II 6245.637 Å line is used to derive Sc abundance in HE 0457−1805; Sc II 6245.637 and 6604.601 Å lines were used in HE 0920−0506. The Sc II lines at 4320.732 and 4415.556 Å were used in HE 1241−0337. In the case of HE 1327−2116, Sc II 4374.457 and 5031.021 Å lines were used. In HE 0920−0506 and HE 1327−2116, scandium is

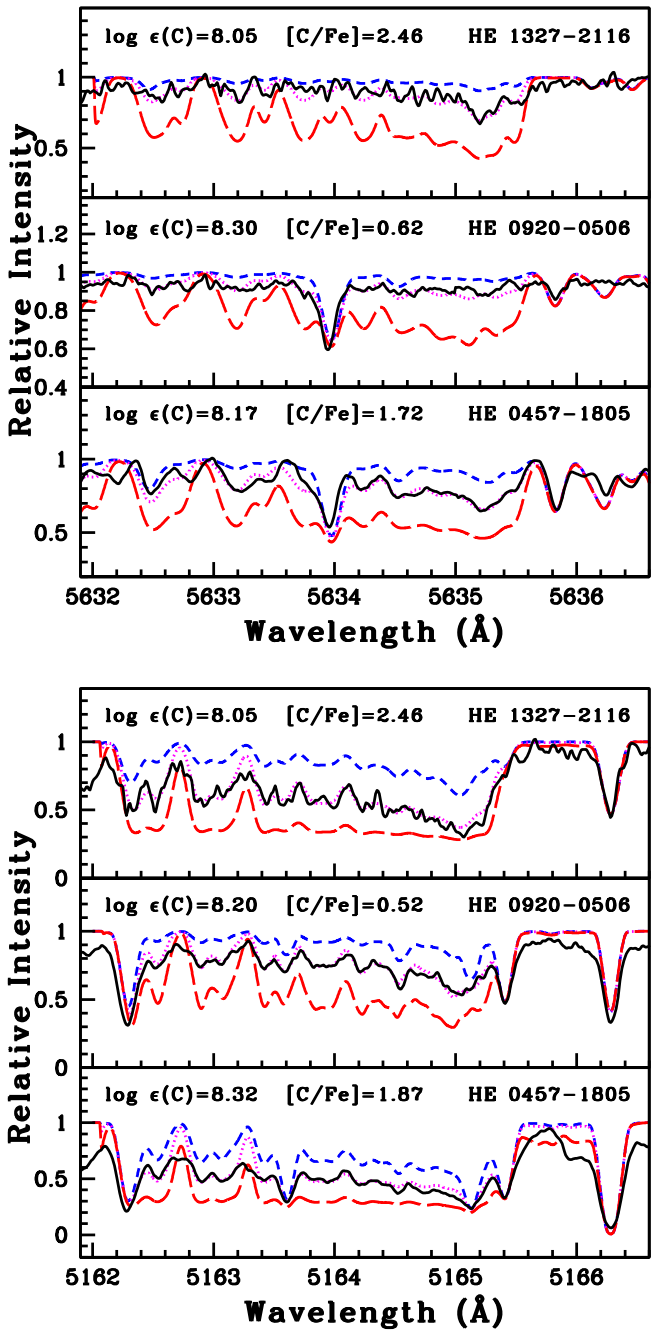

Figure 4. Spectral synthesis fits of the C_2 band around 5165 Å (lower panel) and 5635 Å (upper panel). Dotted and solid lines respectively represent synthesized and observed spectra; short-dashed and long-dashed lines are the synthetic spectra for Δ[C/Fe] = −0.3 and +0.3, respectively.

slightly underabundant with [Sc/Fe] ∼ −0.25, while it is moderately enhanced in the other two stars. Vanadium abundance is derived from the spectral synthesis calculation of V I 4864.731 and 5727.048 Å lines. We could not estimate vanadium abundance in HE 1241−0337 and HE 1327−2116 because there are no clean lines available. The objects HE 0457−1805 and HE 0920−0506 show [V/Fe] values of 0.78 and −0.31, respectively. Manganese abundance is derived from the spectral synthesis calculation of Mn I 6013.513 and 6021.89 Å lines in the stars HE 0457−1805 and HE 0920−0506. The Mn I 5516.743 Å line is used in HE 1241−0337, and Mn I lines at 4451.586 and 4470.140 Å were used in the case of HE 1327−2116. We have used the Co I 4118.770, 4121.320, 5342.695, and 5483.344 Å lines to estimate the cobalt abundance. We could not estimate the cobalt abundance in HE 1241−0337 because no good lines were found in the spectrum. The cobalt abundances, [Co/Fe], in the program stars are in the range from −0.34 to +0.57. Copper abundance is derived using the line Cu I 5105.537 Å.

5.2. Heavy Elements

5.2.1. The Light s-process Elements: Rb, Sr, Y, Zr

The rubidium abundance is derived from the spectral synthesis calculation of the Rb I resonance line at 7800.259 Å. The HFS components of this line are taken from Lambert & Luck (1976). The other Rb I line at 7947.597 Å was not usable for abundance determination in any of the program stars. We could not derive the Rb abundance in HE 1241−0337 because this region is absent from the spectrum, or in HE 1327−2116 because we could not detect any good lines due to Rb. While Rb is found to be enhanced in HE 0457−1805 with [Rb/Fe] ∼ 1.41, it shows a near-solar value in HE 0920−0506.

We have estimated the Sr abundance using the spectral synthesis calculation of the Sr I 4607.327 Å line. This line is known to be affected by the NLTE effect, and the appropriate NLTE corrections are adopted from Bergemann et al. (2012). The Sr abundance could be determined in all the program stars except HE 1327−2116, and it is found to be enhanced with [Sr/Fe] > 1.10. The NLTE corrections to the abundances of Sr for HE 0457−1805 and HE 1241−0337 are +0.47, and that for HE 0920−0506 is +0.17.

Yttrium abundance is derived from the spectral synthesis calculation of the Y I 6435.004 Å line and from the measured equivalent widths of several Y II lines listed in Table A2. While we could estimate Y II abundance in all the program stars, Y I abundance could not be determined in HE 1241−0337 or HE 1327−2116 because we could not detect any good Y I lines. The Y II abundance, [Y II/Fe], ranges from 0.69 to 1.95, whereas Y I abundances, [Y I/Fe], are 2.78 and 0.86, respectively, in HE 0457−1805 and HE 0920−0506.

We have estimated the Zr abundance from the spectral synthesis calculation of the Zr I 6134.585 Å line in all the stars. The Zr II abundance is derived from the measured equivalent widths of several Zr II lines in HE 1241−0337 and spectral synthesis of the Zr II 5112.297 Å line in the other three program stars. While Zr I abundances, [Zr I/Fe], range from 1.22 to 2.43, Zr II abundances, [Zr II/Fe], range from 0.55 to 2.03.

5.2.2. The Heavy s-process Elements: Ba, La, Ce, Pr, Nd

In all program stars, the abundance of Ba is derived from the spectral synthesis calculation of the Ba II 5853.668 Å line by incorporating the hyperfine components. The NLTE corrections to the abundances derived from this line are adopted from Andrievsky et al. (2009). The NLTE correction is +0.05 for HE 1241−0337, +0.28 for HE 1327−2116, and 0.00 for the other two stars. We could also use the line Ba II 6496.897 Å in the object HE 0920−0506. In other stars, this line is not usable. The Ba II 4934.076 and 6141.713 Å lines were either strong (equivalent width > 240 mÅ) or not good to be used for abundance determination in all the objects. Ba is found to be enhanced in all the program stars with [Ba/Fe] > 1.0. The

Table 6
Estimates of [ls/Fe], [hs/Fe], [s/Fe], [hs/ls], and [Rb/Zr]

Star Name	[Fe/H]	[ls/Fe]	[hs/Fe]	[s/Fe]	[hs/ls]	[Rb/Zr]
HE 0457−1805	−1.98	1.88	2.38	2.16	0.50	−1.02
HE 0920−0506	−0.75	1.29	1.22	1.15	−0.07	−1.29
HE 1241−0337	−2.47	1.20	1.06	1.31	−0.14	⋯
HE 1327−2116	−2.84	0.92	1.75	1.48	0.83	⋯

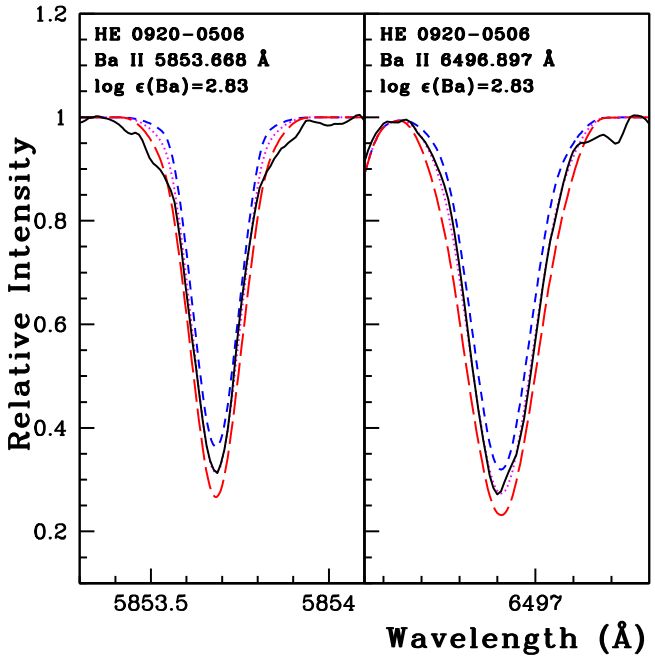

Figure 5. Spectral synthesis fits of Ba II 5853.668 Å and 6496.897 Å lines in the star HE 0920−0506. Synthesized and observed spectra are shown by dotted and solid lines, respectively. Short-dashed and long-dashed lines are the synthetic spectra for Δ[Ba/Fe] = −0.3 and +0.3, respectively.

spectral synthesis fits for Ba II 5853.668 and 6496.897 Å lines for the star HE 0920−0506 are shown in Figure 5.

The La abundance is derived from the spectral synthesis calculation of La II lines at 4748.726, 4921.776, 5259.379, and 5303.528 Å, whenever possible, by incorporating the HFS components. The HFS components of La II 4748.726 and 5259.379 Å lines were not available. All the program stars show enhancement of La with [La/Fe] > 1, HE 0457−1805 being the most enriched in La with a value [La/Fe] ∼ 2.27.

The abundances of Ce, Pr, and Nd are derived using the equivalent widths measured from several lines of the singly ionized species of these elements. The atomic lines used for the abundance determination of these elements are given in Table A2. All the program stars are found to show enhancement of [X/Fe] > 1 for all these elements.

We have also calculated the [ls/Fe], [hs/Fe], and [hs/ls] ratios of the program stars. Here, ls stands for light s-process elements: Sr, Y, and Zr, and hs stands for heavy s-process elements: Ba, La, Ce, and Nd. We have also calculated the [s/Fe] ratio, a measure of the total s-process content of a star, for all the program stars. Here s refers to the s-process elements Sr, Y, Zr, Ba, La, Ce, and Nd. [hs/Fe] is calculated as ([Ba/Fe] + [La/Fe] + [Ce/Fe] + [Nd/Fe])/4, [ls/Fe] as ([Sr/Fe] + [Y/Fe] + [Zr/Fe])/3, and [s/Fe] as ([Sr/Fe] + [Y/Fe] + [Zr/Fe] + [Ba/Fe] + [La/Fe] + [Ce/Fe] + [Nd/Fe])/7. Values of these ratios are given in Table 6. As seen from the table, all our stars have high s-process content with [s/Fe] > 1. We could estimate the [Rb/Zr] ratio, an indicator of neutron density at an s-process site and the mass of a companion AGB star, for two objects. Estimated values of this ratio are also provided in Table 6. These ratios will be discussed in detail later in this paper.

5.2.3. The r-process Elements: Sm, Eu

We have used the measured equivalent widths of several Sm II lines listed in Table A2 to derive the abundance of Sm. All the stars show enhanced abundance of Sm with [Sm/Fe] ⩾ 0.99. The abundance of Eu is derived from the spectral synthesis calculation of the Eu II 6645.064 Å line in all the four program stars. We could also use the Eu II line at 4129.725 Å in HE 0920−0506, and the Eu II 6437.640 Å line in HE 1241−0337. The Eu II 4129.725 Å line is affected by NLTE, and the correction to the abundance derived from this line (∼+0.16) is adopted from Mashonkina et al. (2008). While Eu is mildly underabundant in HE 0920−0506 with [Eu/Fe] ∼ −0.20, it is moderately enhanced in HE 1241−0337 with [Eu/Fe] ∼ 0.52. The other two stars HE 0457−1805 and HE 1327−2116 are enhanced in Eu with [Eu/Fe] value around 1.20.

6. Abundance Uncertainties

The uncertainty in the abundance of each element is calculated following the procedure in Shejeelammal et al. (2020) using

$$\sigma^2_{\log\epsilon} = \sigma^2_{\rm ran} + \left(\frac{\partial\log\epsilon}{\partial T}\right)^2 \sigma^2_{T_{\rm eff}} + \left(\frac{\partial\log\epsilon}{\partial\log g}\right)^2 \sigma^2_{\log g} + \left(\frac{\partial\log\epsilon}{\partial\zeta}\right)^2 \sigma^2_{\zeta} + \left(\frac{\partial\log\epsilon}{\partial[{\rm Fe/H}]}\right)^2 \sigma^2_{\rm [Fe/H]}.$$

Here, $\sigma_{\log\epsilon}$ is the total uncertainty in the absolute abundance of the particular element. $\sigma_{\rm ran}$ is the random error and is calculated from the standard deviation (σ_s) of the abundances derived from N lines of the particular element using $\sigma_{\rm ran} = \sigma_s/\sqrt{N}$. $\sigma_{T_{\rm eff}}$, $\sigma_{\log g}$, σ_ζ, and $\sigma_{\rm [Fe/H]}$ are the typical uncertainties in the stellar atmospheric parameters, which are $\sigma_{T_{\rm eff}} \sim \pm 100$ K, $\sigma_{\log g} \sim \pm 0.2$ dex, $\sigma_\zeta \sim \pm 0.2$ km s^{-1}, and $\sigma_{\rm [Fe/H]} \sim \pm 0.1$ dex. The uncertainty in the abundance ratio of an element, X, is calculated from

$$\sigma^2_{\rm [X/Fe]} = \sigma^2_{\rm X} + \sigma^2_{\rm Fe}.$$

We made the calculation simple by assuming that the parameters are independent. Hence, the uncertainties calculated here are taken to be the upper limits. The changes in the abundances of each element with the variation in different atmospheric parameters are given in Table 7. We have evaluated the differential abundances in the specific case of the star HE 0920−0506.

Table 7
Change in the Abundances ($\Delta\log\epsilon$) of Different Elemental Species (of the Star HE 0920−0506) with Variations in Stellar Atmospheric Parameters (Columns 2–5)

Element	$\Delta T_{\rm eff}$ ($\pm$ 100 K)	$\Delta\log g$ ($\pm$ 0.2 dex)	$\Delta\zeta$ ($\pm$ 0.2 km s^{-1})	Δ [Fe/H] ($\pm$ 0.1 dex)	$\sigma_{\rm [X/Fe]}$
C	±0.07	±0.10	∓0.10	±0.10	0.23
N	±0.13	±0.03	0.00	±0.02	0.19
O	0.00	±0.04	±0.02	0.00	0.14
Na I	±0.04	∓0.01	∓0.02	∓0.01	0.15
Mg I	±0.07	∓0.06	∓0.03	±0.01	0.16
Si I	±0.04	0.00	∓0.02	0.00	0.18
Ca I	±0.08	∓0.04	∓0.07	0.00	0.17
Sc II	∓0.01	±0.08	∓0.04	±0.02	0.19
Ti I	±0.11	∓0.01	∓0.07	∓0.01	0.19
Ti II	∓0.01	±0.06	∓0.10	±0.02	0.18
V I	±0.13	∓ 0.04	∓0.13	0.00	0.23
Cr I	±0.10	∓ 0.03	∓0.09	∓0.01	0.19
Cr II	∓0.04	±0.08	∓0.06	±0.02	0.20
Mn I	±0.08	∓0.01	∓0.08	∓0.01	0.17
Fe I	±0.09	0.00	∓0.09	∓ 0.01	⋯
Fe II	∓0.05	±0.08	∓0.13	±0.03	⋯
Co I	±0.11	0.00	∓0.03	∓0.01	0.17
Ni I	±0.07	∓0.02	∓0.07	∓0.01	0.17
Cu I	±0.11	∓0.02	∓0.16	∓0.01	0.23
Zn I	∓0.01	±0.02	∓0.09	0.00	0.18
Rb I	±0.10	0.00	∓0.03	0.00	0.17
Sr I	±0.11	∓0.04	∓0.18	0.00	0.25
Y I	±0.16	0.00	∓0.01	∓0.01	0.21
Y II	±0.01	±0.05	∓0.14	±0.02	0.23
Zr I	±0.12	0.00	∓0.05	0.02	0.18
Zr II	∓0.01	±0.06	∓0.17	±0.01	0.24
Ba II	±0.05	±0.02	∓0.10	±0.04	0.20
La II	±0.04	±0.03	∓ 0.20	±0.02	0.26
Ce II	±0.02	±0.08	∓0.14	±0.02	0.24
Pr II	±0.03	±0.08	∓0.03	±0.02	0.19
Nd II	±0.03	±0.07	∓0.13	±0.02	0.23
Sm II	±0.03	±0.07	∓0.11	±0.02	0.23
Eu II	∓0.04	±0.07	∓0.26	±0.03	0.27

Note. The total uncertainty in [X/Fe] of each element is given in the sixth column.

7. Classification of the Program Stars

Among our stellar sample, HE 0457−1805, HE 1241−0337, and HE 1327−2116 are found to be metal-poor objects with [Fe/H] < -1, whereas HE 0920−0506 is moderately metal-poor with [Fe/H] ~ -0.75. CEMP stars are traditionally classified as metal-poor stars with [C/Fe] > 1 (Beers & Christlieb 2005). This classification criterion is being refined and many authors use different threshold values for [C/Fe] to define CEMP stars. However, the carbon abundance is related to the evolutionary stages of the stars. In the case of evolved metal-poor giant stars, the surface carbon abundance could be altered through the CNO cycle as a result of internal mixing. This internal mixing processes are first dredge-up on the giant branch and some extra mixing at the tip of the red giant branch (Charbonnel 1995; Charbonnel et al. 1998; Gratton et al. 2000; Shetrone 2003; Jacobson et al. 2005; Spite et al. 2005, 2006; Aoki et al. 2007; Placco et al. 2014). Hence, using a fixed [C/Fe] value to define CEMP stars without considering the evolutionary effects would be incomplete. Here, we have adopted the empirical definition of Aoki et al. (2007) to distinguish the CEMP stars of our sample. This definition is shown schematically in Figure 6. As seen from this figure, while HE 0457−1805 and HE 1327−2116 are CEMP stars, HE 0920−0506 is a non-CEMP star. From the C/O value (>1) of HE 0920−0506, we found that it is a CH star. We could not locate the star HE 1241−0337 in this diagram because we could not determine its luminosity due to the unavailability of parallax. However, the higher [C/Fe] value (∼2.57) of this star places it in the CEMP category.

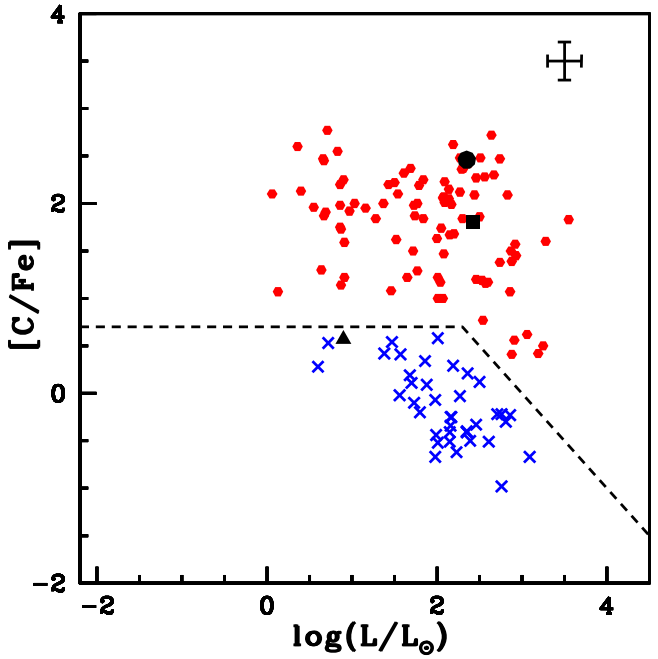

Figure 6. Observed [C/Fe] ratios as a function of stellar luminosity, $\log(L/L_{\odot})$. Red filled hexagons are CEMP stars from the literature (Aoki et al. 2007 and references therein, Goswami et al. 2016). Blue crosses represent carbon-normal metal-poor stars from the literature (Aoki et al. 2005, 2007; Cayrel et al. 2004; Honda et al. 2004). HE 0457−1805 (filled square), HE 0920−0506 (filled triangle), and HE 1327−2116 (filled circle) are marked. The dashed line separates the CEMP and non-CEMP stars. A representative error bar is shown in the top right corner.

We have adopted the classification scheme given by Goswami et al. (2021) to subclassify our CEMP stars. This classification scheme considers [Ba/Eu] and [La/Eu] ratios of the stars, and is given as

1. CEMP-s: [Ba/Fe] $\geqslant 1$
   (i) [Eu/Fe] < 1, [Ba/Eu] > 0, and/or [La/Eu] > 0.5
   (ii) [Eu/Fe] $\geqslant 1$, [Ba/Eu] > 1, and/or [La/Eu] > 0.7
2. CEMP-r/s: [Ba/Fe] $\geqslant 1$, [Eu/Fe] $\geqslant 1$
   (iii) $0 \leqslant$ [Ba/Eu] $\leqslant 1$ and/or $0 \leqslant$ [La/Eu] $\leqslant 0.7$

Figure 7 schematically represents this classification. The values of [C/Fe], [Ba/Eu], and [La/Eu] ratios observed in the program stars are given in Table 8. In Figure 7, the above conditions (i) and (ii) of CEMP-s stars are marked as regions (i) and (ii), respectively, and the CEMP-r/s condition is marked as region (iii). From this figure and Table 8, the objects HE 0457−1805 and HE 1241−0337 are found to be CEMP-s stars (regions (ii) and (i), respectively) and the object HE 1327−2116 is found to be a CEMP-r/s star (region (iii)).

8. Discussion

8.1. Comparison of the Observed Abundances

We have compared the observed abundances of light as well as heavy elements in our program stars with those in CH, Ba, CEMP, and normal stars from the literature, and the results are shown in Figures 8 and 9. All the s-process elements in the program stars show enhanced abundances compared to the normal stars. All the light elements except Na, Mg, V, Cr, Mn, and Ni show abundances similar to those seen in normal stars of the Galaxy. In HE 0457−1805 the elements Na, Mg, V, Cr, Mn, and Ni are enhanced when compared to normal giants. Similarly, Mn and Ni are enhanced in HE 1327−2116. Similar enhancements of Na, Mg, and/or Fe-peak elements in CEMP stars were reported in the literature (Aoki et al. 2006; Frebel et al. 2008; Bessell et al. 2015; Shejeelammal & Goswami 2021; Goswami et al. 2021; Purandardas & Goswami 2021). Several sources such as faint SNe, spinstars, and AGB mass transfer combined with metal accretion from the ISM have been used to explain their abundance patterns (Aoki et al. 2006; Frebel et al. 2008; Bessell et al. 2015). According to Choplin et al. (2017), multiple sources may contribute to the formation of CEMP stars. This may be a possible reason for the observed enhancement of these elements. It is possible that the natal clouds of the CEMP stars might get polluted from multiple faint SNe events in the past. A study by Hartwig et al. (2018) has presented a number of reliable tracers to identify whether the natal clouds of CEMP stars are mono- or multi-enriched. According to them, the elemental ratios $[Mg/C] < 1$, $[Sc/Mn] < 0.5$, $[C/Cr] > 0.5$ or $[Ca/Fe] > 2$ indicates mono-enrichment. We found $[Ca/Fe] < 2$ in our program stars HE 0457−1805 and HE 1327−2116, which may indicate that these stars were formed from a gas cloud enriched by multiple SNe events. This may also be a possible reason for the enhanced abundances of the above-mentioned elements in these stars. Enhanced Na and/or Mg abundances are observed in a few CEMP-s and CEMP-r/s stars (Bisterzo et al. 2011; Allen et al. 2012; Karinkuzhi et al. 2021; Goswami et al. 2021; Shejeelammal & Goswami 2021). We discuss the Na and Mg abundances in detail in Section 8.3.2.

8.2. Carbon Abundance and Possible Origin of Program Stars

Studies have shown that the absolute carbon abundances, A(C), of CEMP stars show bimodality, that is they tend to plateau around two distinct A(C) values in the A(C)–[Fe/H] diagram (Spite et al. 2013; Bonifacio et al. 2015; Hansen et al. 2015; Yoon et al. 2016). The CEMP-s and CEMP-r/s stars populate the high-carbon band at $A(C) \sim 7.96$ and the CEMP-no stars populate the low-carbon band at $A(C) \sim 6.28$. This bimodal behavior is due to the difference in the origin of carbon in the stars of these two bands. The carbon observed in the stars of the high-carbon band (CEMP-s and CEMP-r/s) has an extrinsic origin: binary mass transfer from a low-mass AGB star, whereas the carbon in the stars of the low-carbon band (CEMP-no) has an intrinsic[3] origin: pre-enrichment of their natal cloud by faint SNe, spinstars, or metal-free massive stars (Spite et al. 2013; Bonifacio et al. 2015; Yoon et al. 2016 and references therein). This interpretation is in agreement with the results of many radial velocity monitoring studies of CEMP stars. The majority of CEMP-s and CEMP-r/s stars are found to be binaries, and a large fraction of CEMP-no stars are found to be single (Lucatello et al. 2005; Starkenburg et al. 2014; Jorissen et al. 2016a; Hansen et al. 2016a, 2016b; Arentsen et al. 2019). The binary fraction of CEMP-s and CEMP-r/s stars is found to be 82% ± 10% (18 out of 22 stars,

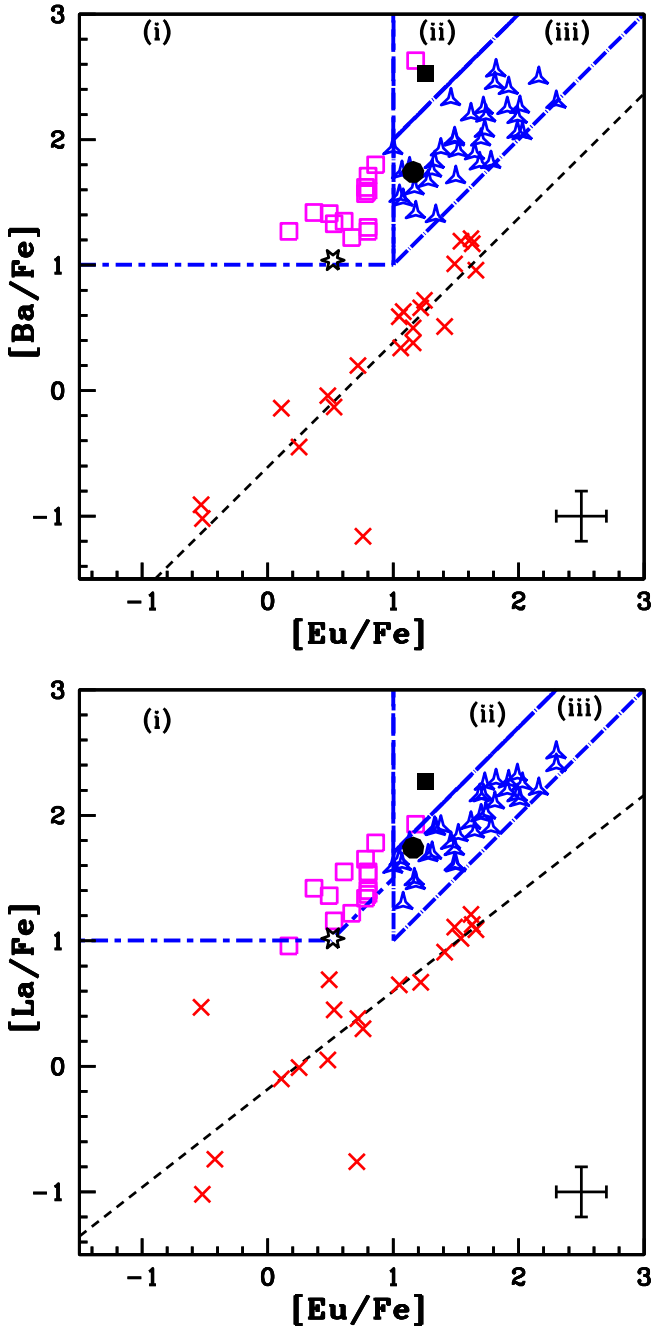

Figure 7. Observed [Ba/Fe] (upper panel) and [La/Fe] (lower panel) as functions of observed [Eu/Fe] for CEMP and r-stars. Magenta squares are CEMP-s stars, blue starred triangles are CEMP-r/s stars, and red crosses are r-stars (including both CEMP-r and rI/rII stars) from the literature (Masseron et al. 2010; Shejeelammal et al. 2021; Shejeelammal & Goswami 2021; Karinkuzhi et al. 2021; Goswami et al. 2021). HE 0457−1805 (filled square), HE 1241−0337 (six-sided star), and HE 1327−2116 (filled circle) are marked. Regions (i) and (ii) are the CEMP-s stars and region (iii) is CEMP-r/s stars (Goswami et al. 2021). The least-squares fit to the abundances observed in r-stars is shown by the dashed line. A representative error bar is shown in the bottom right corner of each panel.

[3] We used the term intrinsic to indicate that the observed abundance pattern of the star is the actual chemical imprint of the gas cloud from which the star is formed, and not the self-enrichment of the star.

Table 8
[C/Fe], [Ba/Eu], and [La/Eu] Ratios in the Program Stars

Star Name	[Fe/H]	[C/Fe]	[Ba/Fe]	[La/Fe]	[Eu/Fe]	[Ba/Eu]	[La/Eu]
HE 0457−1805	−1.98	1.80	2.53	2.27	1.26	1.43	1.01
HE 0920−0506	−0.75	0.57	1.40	1.25	−0.20	1.60	1.45
HE 1241−0337	−2.47	2.57	1.04	1.02	0.52	0.52	0.50
HE 1327−2116	−2.84	2.46	1.74	1.74	1.16	0.58	0.58

Hansen et al. 2016b) and that of CEMP-no stars is 17% ± 9% (4 out of 24 stars, Hansen et al. 2016a).

From the compilation of a sample of CEMP stars from the literature, Yoon et al. (2016) have proposed that the carbon abundance $A(C) \sim 7.1$ could separate binary stars from single stars in the A(C)–[Fe/H] diagram, though there are a few outlier stars. The majority of binary stars lie above this absolute carbon abundance value. A study by Arentsen et al. (2019) on a sample of CEMP-no stars also confirmed the relation between high carbon abundance and the binarity of metal-poor stars. Hence, we have used this diagram to get an idea about the binary status of our program stars.

However, before using the estimated carbon abundance for this diagram, the appropriate correction should be applied to it in order to account for any internal mixing. Internal mixing tends to alter the surface carbon abundance through the CNO cycle. Hence the [C/N] and $^{12}C/^{13}C$ ratios could be used as mixing diagnostics. Mixed stars show [C/N] < -0.6 (Spite et al. 2005) and $^{12}C/^{13}C < 10$ (Spite et al. 2006). However, the carbon isotopic ratio is the better indicator since the carbon and nitrogen abundances in the ISM show larger variations (Spite et al. 2006). The $^{12}C/^{13}C$ ratio is not available for HE 0920−0506 and HE 1241−0337. All our program stars show [C/N] < -0.6, indicating that none of them are mixed. However, the object HE 1327−2116 shows $^{12}C/^{13}C \sim 7$, which indicates internal mixing. The corrections to the observed absolute carbon abundances are calculated using the public online tool developed by Placco et al. (2014), which is available at http://vplacco.pythonanywhere.com/. The correction factors are 0.08, 0.03, 0.06, and 0.10, respectively, for HE 0457−1805, HE 0920−0506, HE 1241−0337, and HE 1327−2116. The corrected A(C) values are used to locate the program stars in A(C)–[Fe/H] diagram, which is shown in Figure 10. We have included only those CEMP stars from the literature whose binary status is known. Binary CH and Ba stars from the literature are also included in the figure to show their position.

All the four program stars lie in the high-carbon band. While HE 0920−0506 lies among other CH stars, the other three stars lie among CEMP-s and CEMP-r/s stars. As seen from the figure, all the stars belong to the region of binary stars. Hence, we may expect that all the program stars are likely binaries. This, combined with the discussion on radial velocities of the program stars in Section 3, may therefore point at the pollution from binary companions.

8.3. Nature of Companion AGB Stars of the Program Stars

We have seen from the previous section that the program stars are likely binaries. In this section, we discuss the nature of the companion AGB stars from the analysis of different abundance profiles of the program stars.

8.3.1. The [hs/ls] Ratio

The ratio of abundances of heavy s-process elements to the light s-process elements, [hs/ls], is an indicator of s-process efficiency in AGB stars. The AGB models predict a positive value for this ratio in low-mass AGB stars ($\leqslant 3\ M_{\odot}$) and a negative value in the case of massive AGB stars ($>3\ M_{\odot}$) (Busso et al. 2001; Goriely & Siess 2005; Karakas 2010; Karakas et al. 2012; van Raai et al. 2012; Karakas & Lattanzio 2014). As seen from Table 6, while the stars HE 0457−1805 and HE 1327−2116 show positive values for [hs/ls] (0.50 and 0.83, respectively), HE 0920−0506 and HE 1241−0337 show negative values, ∼−0.07 and −0.14, respectively. This implies that mainly light s-process elements are produced rather than heavy s-process elements, which are characteristic of massive AGB stars. However, negative values for this ratio have been reported in the literature for a few stars whose companions are found to be low-mass AGB stars from the comparison of observed abundances and AGB nucleosynthesis models (Aoki et al. 2002; Bisterzo et al. 2011; Hansen et al. 2019; Shejeelammal & Goswami 2021). In massive AGB stars, nitrogen is enhanced compared to carbon as a result of hot-bottom burning (HBB) (e.g., McSaveney et al. 2007; Johnson et al. 2007; Karakas & Lattanzio 2014). However, in HE 0920−0506 and HE 1241−0337 the observed [C/N] values are ∼0.12 and 1.55, respectively. This observed C and N abundances in HE 0920−0506 and HE 1241−0337 may therefore rule out the possibility of a massive AGB companion.

8.3.2. Na, Mg, and Heavy Elements

In massive AGB stars with HBB, besides N, sodium is also expected to be produced in abundance through the Ne–Na cycle (e.g., Mowlavi 1999). The $^{22}Ne(\alpha, n)^{25}Mg$ reaction in massive AGB stars results in an enhanced abundance of Mg too (e.g., Karakas & Lattanzio 2003). Among our program stars, three stars are enhanced in Na: HE 1327−2116 with [Na/Fe] ∼ 0.88, HE 1241−0337 with [Na/Fe] ∼ 1.58, and HE 0457−1805 with [Na/Fe] ∼ 2.20. The star HE 0457−1805 is also enhanced in magnesium with [Mg/Fe] ∼ 1.32. However, the [hs/ls] ratio (∼0.50) and [C/N] value (∼0.13) of HE 0457−1805 and the higher [C/N] ratio of HE 1241−0337 (∼1.55) rule out the possibility of a massive AGB companion. A few other studies have already reported such higher enhancement of Na and/or Mg in CEMP stars, for instance, CS 29528−028, [Fe/H] ∼ −2.86, [Na/Fe] ∼ 2.68, [Mg/Fe] ∼ 1.69 (Aoki et al. 2007), SDSS 1707+58, [Fe/H] ∼ −2.52, [Na/Fe] ∼ 2.71, [Mg/Fe] ∼ 1.13 (Aoki et al. 2008), and HE 1304−2111, [Fe/H] ∼ −2.34, [Na/Fe] ∼ 2.83 (Shejeelammal & Goswami 2021). The star HE 1304−2111 is found to have a low-mass AGB companion from a detailed abundance analysis (Shejeelammal & Goswami 2021). Bisterzo et al. (2011) have analyzed the observed abundances in a sample of CEMP-s stars (∼100 objects) from the literature using the AGB models of Bisterzo

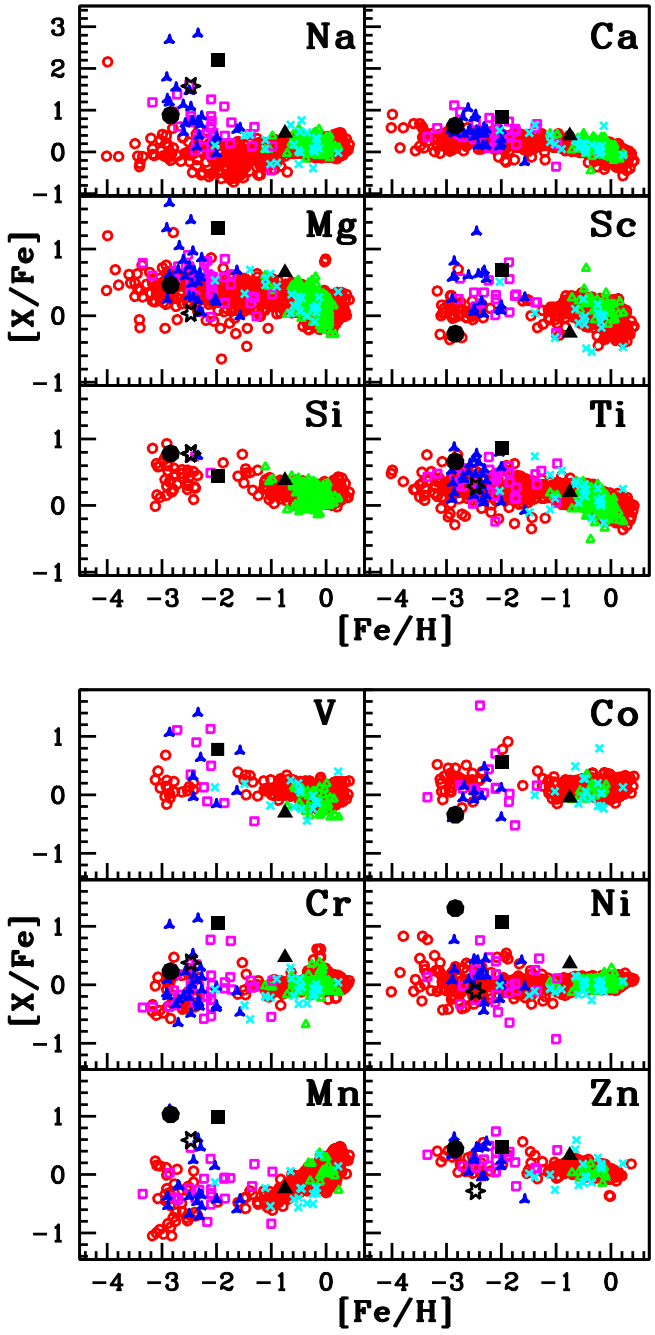

Figure 8. Observed [X/Fe] ratios of the light elements in the program stars with respect to metallicity [Fe/H]. Red open circles correspond to normal giants from the literature (Honda et al. 2004; Venn et al. 2004; Aoki et al. 2005, 2007; Reddy et al. 2006; Luck & Heiter 2007; Hansen et al. 2016c; Yoon et al. 2016). Magenta open squares and blue starred triangles represent CEMP-s and CEMP-r/s stars, respectively, from the literature (Masseron et al. 2010; Purandardas et al. 2019; Karinkuzhi et al. 2021; Shejeelammal et al. 2021; Shejeelammal & Goswami 2021; Goswami et al. 2021; Purandardas & Goswami 2021). Cyan crosses represent CH stars from the literature (Vanture 1992; Karinkuzhi & Goswami 2014, 2015; Goswami et al. 2016; Shejeelammal et al. 2021; Shejeelammal & Goswami 2021). Green open triangles are Ba stars from the literature (Allen & Barbuy 2006; de Castro et al. 2016; Yang et al. 2016; Karinkuzhi et al. 2018; Shejeelammal et al. 2020). HE 0457−1805 (filled square), HE 0920−0506 (filled triangle), HE 1241−0337 (six-sided star), and HE 1327−2116 (filled circle) are marked.

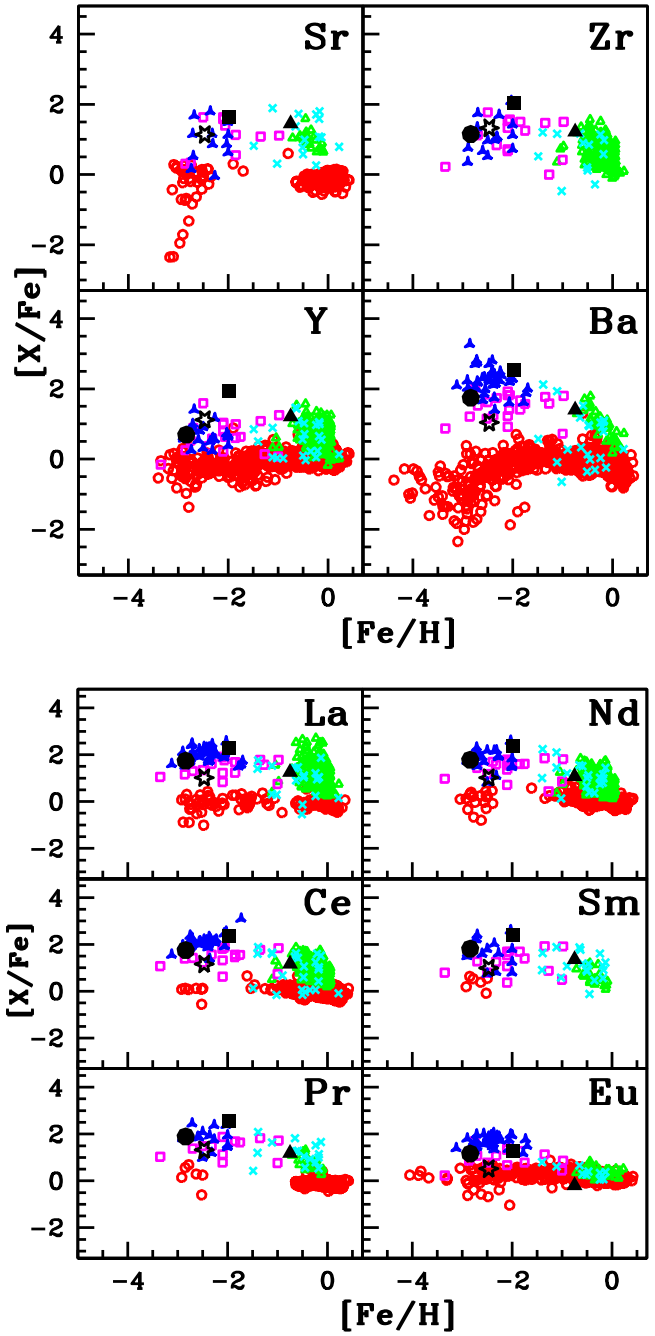

Figure 9. Observed [X/Fe] ratios of the heavy elements in the program stars with respect to metallicity [Fe/H]. Symbols have the same meaning as in Figure 8.

et al. (2010). These AGB models have considered ^{23}Na and ^{24}Mg to be primary, produced through ^{22}Ne(n, γ)^{23}Ne($\beta^{-}\nu$)^{23}Na and ^{23}Na(n, γ)^{24}Na($\beta^{-}\nu$)^{24}Mg. If the ^{23}Na produced is primary, a larger amount of it would be expected (Mowlavi 1999; Gallino et al. 2006). These models predicted high Na abundances at low metallicities. The analysis of Bisterzo et al. (2011) has shown that the higher Na abundances of CS 29528−028 and SDSS 1707+58 could be reproduced with AGB models of $M^{\rm ini}_{\rm AGB} \sim 1.5\ M_{\odot}$. Their higher [ls, hs/Fe] values could be reproduced with $M^{\rm ini}_{\rm AGB} \sim 2.0\ M_{\odot}$ models. The entire observed abundance pattern could not be reproduced with the same AGB model.

In AGB models, considering the partial mixing of protons, ^{23}Na is produced efficiently, almost 50 more so than in the H-burning shell (Goriely & Mowlavi 2000). In such a scenario, Na is produced in the inter-shell in a region above the region of

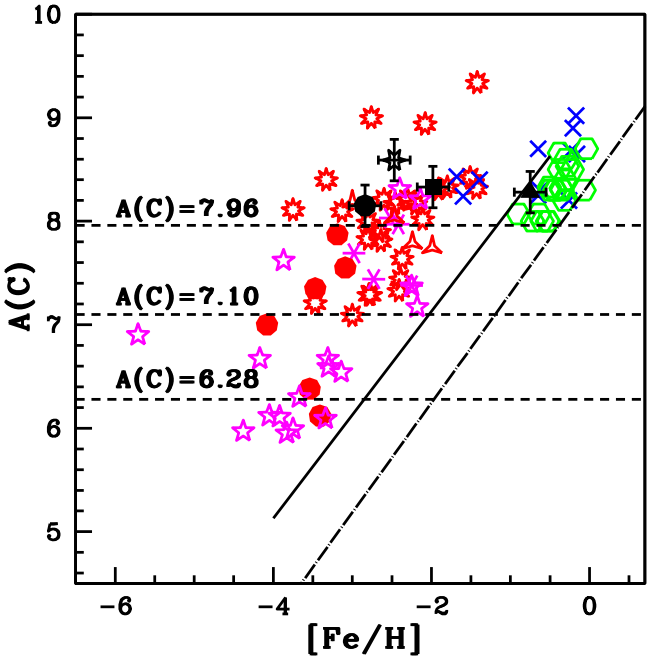

Figure 10. Distribution of A(C) as a function of [Fe/H] for confirmed/likely binary CEMP stars from the literature (Yoon et al. 2016): binary CEMP-s (red nine-sided stars), single CEMP-s (magenta six-sided crosses), binary CEMP-r/s (red starred triangles), binary CEMP-no (red filled circles), and single CEMP-no (magenta five-sided stars). All the red symbols correspond to binary CEMP stars and magenta symbols to single CEMP stars. Blue crosses represent the binary CH stars from the literature (Purandardas et al. 2019; Karinkuzhi & Goswami 2014, 2015; Luck 2017). Binary Ba stars from the literature (Karinkuzhi et al. 2018; Shejeelammal et al. 2020) are represented by green open hexagons. HE 0457−1805 (filled square), HE 0920−0506 (filled triangle), HE 1241−0337 (six-sided star), and HE 1327−2116 (filled circle) are marked. The black dashed line at A(C) = 7.10 separates binary and single stars. The high-carbon (A(C) ∼ 7.96) and low-carbon (A(C) ∼ 6.28) bands of CEMP stars are also shown. The solid line is for [C/Fe] = 0.70 and the long-dashed–dotted line represents the solar carbon value, [C/Fe] = 0.

the s-process, and a correlation between [Na/Fe] and [s/Fe] is expected. This will depend entirely on the extent of the partial mixing zone. However, these models could not explain the least Na-enriched CEMP-s and most Na-enriched CEMP-r/s stars (Figure 19 of Karinkuzhi et al. 2021). Better models with improved simulations are needed to explain these.

8.3.3. The [Rb/Zr] Ratio

Based on the C and N abundances, [hs/ls] ratio, and Na and Mg abundances in the program stars, we have ruled out the possibility of massive AGB companions for our program stars. We have tried to establish an upper limit to the companion's mass from the neutron-density-dependent [Rb/Zr] ratio. Massive AGB stars ($M \geqslant 4\ M_{\odot}$) are characterized by positive values of [Rb/Zr] and low-mass AGB stars ($M \leqslant 3\ M_{\odot}$) by negative values (Abia et al. 2001; van Raai et al. 2012; Karakas et al. 2012). Detailed discussion on [Rb/Zr] ratio is presented in Shejeelammal et al. (2020). We could estimate the value of this ratio in HE 0457−1805 and HE 0920−0506. Both stars show a negative value for this ratio (<−1, Table 6). A comparison of observed Rb and Zr abundances of the program stars with their counterparts in intermediate-mass AGB stars of the Galaxy and Magellanic Clouds is shown in Figure 11. The Rb and Zr abundances of AGB stars are taken from van Raai et al. (2012). It is clear from the figure that the [Rb/Fe] and [Zr/Fe] observed in the program stars do not match closely

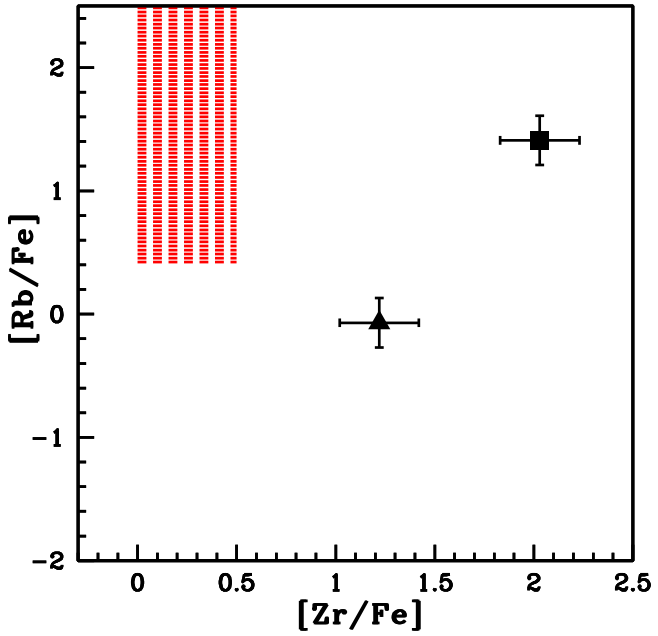

Figure 11. The observed [Rb/Fe] and [Zr/Fe] in the program stars HE 0457−1805 (filled square) and HE 0920−0506 (filled triangle). The shaded region indicates the observed ranges of [Rb/Fe] and [Zr/Fe] in intermediate-mass AGB stars of the Galaxy and the Magellanic Clouds (van Raai et al. 2012).

with their counterparts observed in the intermediate-mass AGB stars. This confirms the low-mass nature of the companion AGB stars.

8.4. Parametric Model-based Analysis

Our analysis based on different abundance ratios of the program stars has confirmed the pollution from low-mass AGB companions. To corroborate our results, we have conducted a parametric model-based analysis for our sample. The observed abundances of neutron-capture elements in our program stars are compared with the predictions of stellar nucleosynthesis models appropriate for each class of star, which we will discuss here.

8.4.1. CEMP-s and CH Stars

For the objects HE 0457−1805, HE 1241−0337 (CEMP-s), and HE 0920−0506 (CH), the observed abundances are compared with the predicted abundances for the s-process in AGB stars from FRUITY (FRANEC Repository of Updated Isotopic Tables & Yields) models (Cristallo et al. 2009, 2011, 2015). The FRUITY models are available for the range of metallicities from $z = 0.000020$ to 0.020 and for the mass range from 1.3 to 6.0 $M_{\odot}$, and are publicly accessible at http://fruity.oa-teramo.inaf.it/. We have derived the mass of AGB companions of these three stars by minimizing χ^2 between observed and predicted abundances, using the parametric model function of Husti et al. (2009). The dilution experienced by the material on the surface of the program stars is also incorporated in the calculation. The detailed procedure is discussed in Shejeelammal et al. (2020). The best fits obtained for the observed abundance patterns in these stars are shown in Figure 12. The former AGB companions of HE 0457−1805, HE 0920−0506, and HE 1241−0337 are found to have masses of 2.0, 2.5, and 1.5 $M_{\odot}$, respectively.

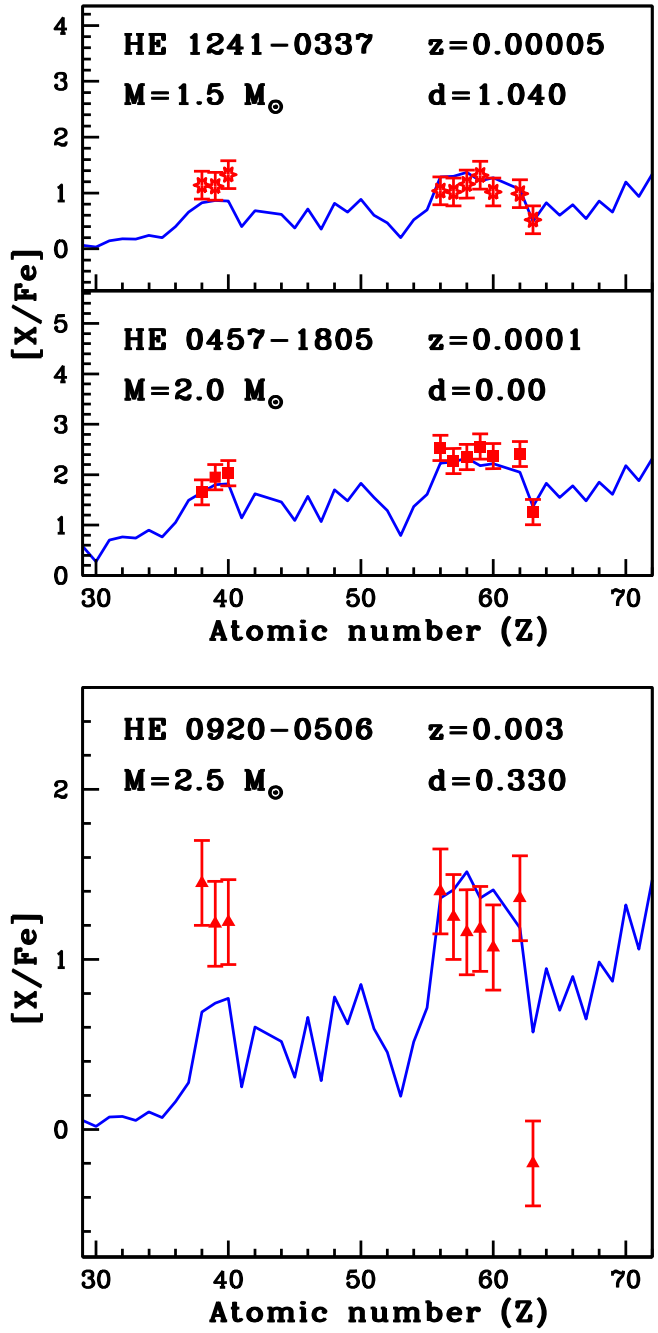

Figure 12. The parametric model fits for the CEMP-s stars, HE 0457−1805 and HE 1241−0337 (upper panel), and CH star HE 0920−0506 (lower panel) using the FRUITY models. Solid curves represent the best fit for the parametric model function. The points with error bars indicate the observed abundances. In the figure, z is the metallicity of the FRUITY model used, and d is the dilution factor, a free parameter that is varied to find the best fit between the model and the observed abundance.

8.4.2. CEMP-r/s Stars

Among a number of scenarios proposed for the origin of CEMP-r/s stars (see, for example, Jonsell et al. 2006 and references therein), several studies have shown that the i-process in low-mass, low-metallicity AGB stars is a promising mechanism to explain their origin (e.g., Hampel et al. 2016, 2019; Karinkuzhi et al. 2021; Goswami et al. 2021; Shejeelammal et al. 2021; Shejeelammal & Goswami 2021; Purandardas & Goswami 2021). Here, we have compared the

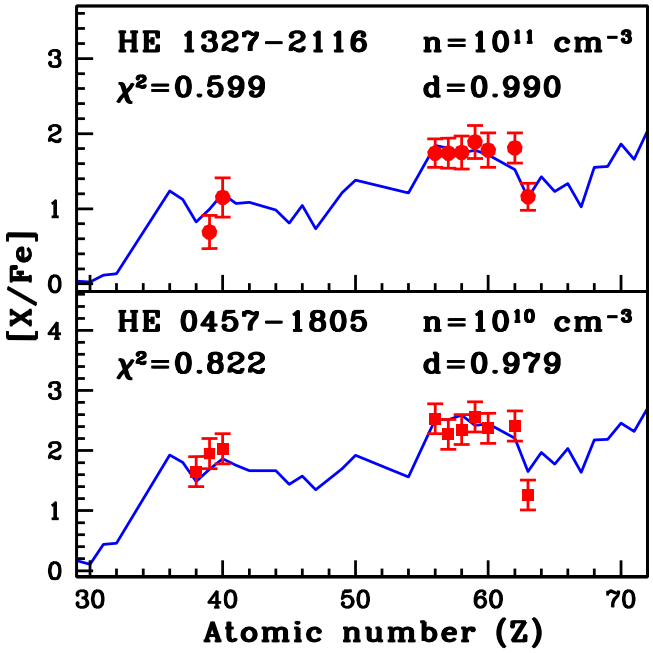

Figure 13. The parametric model fits for HE 0457−1805 (CEMP-s) and HE 1327−2116 (CEMP-r/s) using the i-process model yields (Hampel et al. 2016). Solid curves represent the best fit for the parametric model function. The points with error bars indicate the observed abundances.

observed abundances in our CEMP-r/s star HE 1327−2116 with the i-process model yields of Hampel et al. (2016). The analysis is performed for a range of neutron densities from $n \sim 10^{9}$ to 10^{15} cm^{-3} using the parametric model function given in Hampel et al. (2016), following the procedure discussed in Shejeelammal & Goswami (2021). The best fit obtained for the observed abundance pattern in HE 1327−2116 is shown in Figure 13. We found that the abundance pattern in this star could be reproduced with the i-process models of neutron density $n \sim 10^{11}$ cm^{-3}. We also found that the abundance pattern of the CEMP-s star HE 0457−1805 of our sample could be reproduced with a neutron density $n \sim 10^{10}$ cm^{-3}, indicating the s-process. The parametric model fit for this star is also shown in Figure 13.

8.5. Discussion on Individual Stars

HE 0457−1805. This object is listed among the faint high-latitude carbon stars identified from the Hamburg/ESO Survey (Christlieb et al. 2001). Goswami (2005) identified HE 0457−1805 as a potential CH star candidate from low-resolution spectroscopic analysis. It is found to be a metal-poor star with [Fe/H] ~ -1.98. Our analysis shows that HE 0457−1805 is a CEMP-s star. Kennedy et al. (2011) have reported the stellar atmospheric parameters and C and O abundances of this object from medium-resolution ($R \sim 3000$) optical and near-IR spectroscopic analysis. Our estimates of atmospheric parameters are in agreement with Kennedy et al. (2011) except for [Fe/H], which is 0.5 dex higher than our estimate. They have reported a [C/Fe] value that is ∼0.81 dex lower than our estimate.

HE 0920−0506 and HE 1327−2116. These objects belong to the sample of bright metal-poor candidates selected from the HES (Frebel et al. 2006) through medium-resolution ($R \sim 2000$) spectroscopic analysis. Frebel et al. (2006) have derived the metallicities of these objects from the Ca II K

3933 Å line using the calibration equation of Beers (1999). Within the error limits, these estimates agrees with our metallicity values. A more refined analysis of Beers et al. (2017) using the same medium-resolution spectra as Frebel et al. (2006) had reported the stellar atmospheric parameters ($T_{\rm eff}$, log g, [Fe/H]) ∼ (5291 K, 2.99, −1.39) and (4868 K, 0.55, −3.48), respectively, for HE 0920−0506 and HE 1327−2116. In the case of HE 0920−0506, while our estimate of temperature agrees with theirs, our estimates of surface gravity is ∼0.34 dex lower and the metallicity is ∼0.64 dex higher. In the case of HE 1327−2116, the temperature estimates are in agreement, whereas our estimates of metallicity and surface gravity, respectively, are 0.64 and 0.95 dex higher than their estimates. These differences in the atmospheric parameters may be due to the difference in the method adopted for their determination and also due to the different resolutions of the spectra used. While Frebel et al. (2006) reported the carbon abundances [C/Fe] ∼ 0.09 and 1.11, respectively, for HE 0920−0506 and HE 1327−2116, Beers et al. (2017) reported [C/Fe] ∼ 1.19 and 2.64. Our estimates of carbon abundance for these two stars are [C/Fe] ∼ 0.57 and 2.46, respectively. From our analysis, we found that HE 0920−0506 is a CH star and HE 1327−2116 is a CEMP-r/s star.

HE 1241−0337. This object belongs to the catalog of faint high-latitude carbon stars identified from the Hamburg/ESO Survey (Christlieb et al. 2001). We present the first abundance analysis for this object. We found from our analysis that this object is a CEMP-s star with [Fe/H] ∼ −2.47 and [C/Fe] ∼ 2.57. This object is found to have a high radial velocity. Parametric model-based analysis shows that the former AGB companion of HE 1241−0337 is a low-mass star with mass ∼1.5 $M_{\odot}$.

9. Conclusions

The results of a detailed spectroscopic analysis of four potential CH/CEMP star candidates selected from the Hamburg/ESO Survey are presented. We present the first ever abundance analysis for the object HE 1241−0337. Although the abundances of Fe and C (and O for HE 0920−0506) derived from medium-resolution spectra are available in the literature, we present for the first time a high-resolution spectroscopic analysis for the objects HE 0457−1805, HE 0920−0506, and HE 1327−2116. We have estimated the stellar atmospheric parameters as well as the abundances of 28 elements along with the carbon isotopic ratio.

Our analysis has shown that the objects HE 0457−1805 and HE 1241−0337 are CEMP-s stars, HE 0920−0506 is a CH star, and HE 1327−2116 is a CEMP-r/s star. The estimate of radial velocity shows that HE 0457−1805 and HE 0920−0506 have low radial velocity (<100 km s^{-1}), whereas HE 1241−0337 and HE 1327−2116 have high radial velocity (>100 km s^{-1}). While HE 0457−1805 is a confirmed binary, the difference noted in the radial velocity of HE 0920−0506 from the literature value may indicate that it is likely a binary. Our analysis based on absolute carbon abundance has revealed that all these stars belong to the region of binary stars.

The positions of program stars on the A(C)–[Fe/H] diagram suggest that the observed enhancement in the abundances of the neutron-capture elements may be due to the pollution from binary companions. We have investigated the nature of the companion AGB stars of our program stars using several diagnostics such as C, N, Na, and Mg abundances, and [hs/ls] and [Rb/Zr] ratios. From the analysis based on these diagnostics, we have found that none of the program stars are polluted by massive AGB stars. Our analysis based on different abundance ratios and abundance profiles confirmed the low-mass AGB companions of the program stars.

We have carried out a parametric model-based analysis for the CEMP-s (HE 0457−1805 and HE 1241−0337) and CH (HE 0920−0506) stars in our sample. A comparison of the observed abundances in these stars with the predictions from the FRUITY models of AGB stars by means of a parametric model function incorporating a dilution factor confirmed that the AGB stars that polluted them were low-mass stars with masses $M \leqslant 2.5\ M_{\odot}$.

The observed abundance pattern in the CEMP-r/s star of our sample, HE 1327−2116, is well reproduced with the i-process parametric models in low-mass, low-metallicity AGB stars. The neutron density responsible for its observed abundance is found to be $n \sim 10^{11}$ cm^{-3}. Our analysis for HE 0457−1805 using these same models has shown that the neutron density $n \sim 10^{10}$ cm^{-3} in low-mass AGB stars could reproduce its observed abundance. Thus, the parametric model-based study for the program stars corroborates the results we have obtained from the abundance profile analysis.

Funding from the DST SERB project No. EMR/2016/005283 is gratefully acknowledged. We are thankful to the referee for useful comments and suggestions. We are thankful to Melanie Hampel for providing us with the i-process yields in the form of number fractions. We thank Alain Jorissen for sharing the HERMES spectra used in this study. The HERMES spectrograph is supported by the Fund for Scientific Research of Flanders (FWO), the Research Council of K.U. Leuven, the Fonds National de la Recherche Scientifique (F.R.S.- FNRS), Belgium, the Royal Observatory of Belgium, the Observatoire de Genève, Switzerland, and the Thüringer Landessternwarte Tautenburg, Germany. This work made use of the SIMBAD astronomical database, operated at CDS, Strasbourg, France, and the NASA ADS, USA. This work has made use of data from the European Space Agency (ESA) mission Gaia (https://www.cosmos.esa.int/gaia), processed by the Gaia Data Processing and Analysis Consortium (DPAC, https://www.cosmos.esa.int/web/gaia/dpac/consortium).

Data Availability

The data underlying this article will be shared on reasonable request to the authors.

Line list

The lines used to derive the elemental abundances are listed in Tables A1–A3.

Table A1
Equivalent Widths (in mÅ) of Fe Lines Used for Deriving Atmospheric Parameters

Wavelength (Å)	El.	E_{low} (eV)	log *gf*	HE 0457−1805	HE 0920−0506	HE 1241−0337	HE 1327−2116
4132.9	Fe I	2.85	−1.01	⋯	76.1(6.73)	⋯	⋯
4337.05		1.56	−1.7	145.6(5.42)	⋯	⋯	⋯
4422.568		2.845	−1.11	⋯	74.8(6.69)	⋯	⋯
4531.626		3.211	−2.511	⋯	⋯	⋯	83.4(4.68)
4547.847		3.546	−0.780	⋯	62.6(6.65)	⋯	⋯
4625.045		3.241	−1.34	61.9(5.49)	58.0(6.73)	⋯	⋯
4630.120		2.277	−2.580	⋯	⋯	51.1(5.15)	⋯
4733.591		1.484	−2.71	127.0(5.66)	⋯	⋯	⋯
4924.770		2.277	−2.220	⋯	⋯	67.3(4.95)	⋯
4969.917		4.216	−0.71	⋯	45.3(6.70)	⋯	⋯
4985.253		3.926	−0.440	⋯	⋯	35.4(4.90)	⋯
5005.711		3.883	−0.18	82.8(5.42)	81.3(6.88)	⋯	⋯
5006.119		2.833	−0.61	143.9(5.63)	⋯	⋯	⋯
5044.211		2.849	−2.150	⋯	⋯	23.9(5.01)	⋯
5049.820		2.277	−1.420	⋯	⋯	150.7(5.12)	⋯
5079.223		2.2	−2.067	115.6(5.65)	72.5(6.71)	⋯	27.3(4.72)
5127.359		0.915	−3.307	⋯	80.9(6.78)	⋯	⋯
5151.911		1.010	−3.320	⋯	⋯	137.6(5.05)	⋯
5195.468		4.22	−0.02	71.2(5.49)	74.2(6.83)	⋯	⋯
5198.711		2.222	−2.135	⋯	⋯	⋯	20.6(4.67)
5215.179		3.266	−0.933	⋯	⋯	⋯	20.7(4.69)
5226.862		3.038	−0.667	115.7(5.34)	92.0(6.76)	⋯	45.4(4.57)
5247.05		0.087	−4.946	⋯	53.8(6.70)	⋯	⋯
5307.37		1.61	−2.192	138.7(5.32)	⋯	⋯	⋯
5339.93		3.27	−0.680	117.8(5.66)	⋯	⋯	⋯
5379.574		3.694	−1.480	⋯	40.8(6.78)	⋯	⋯
5393.17		3.24	−0.720	⋯	⋯	⋯	24.2(4.71)
5569.62		3.42	−0.490	⋯	⋯	⋯	31.2(4.66)
5576.089		3.428	−1.000	⋯	⋯	68.88(5.22)	⋯
5701.544		2.557	−2.220	⋯	⋯	49.1(4.94)	⋯
5809.22		3.88	−1.690	⋯	27.4(6.74)	⋯	⋯
5862.357		4.549	−0.051	⋯	61.8(6.71)	⋯	⋯
5956.693		0.858	−4.505	⋯	⋯	48.4(4.98)	⋯
6136.994		2.198	−2.95	⋯	51.0(6.84)	⋯	⋯
6137.694		2.588	−1.403	⋯	⋯	108.5(4.87)	40.4(4.65)
6151.618		2.174	−3.370	⋯	⋯	20.5(5.18)	⋯
6240.646		2.222	−3.380	⋯	38.6(6.78)	⋯	⋯
6252.555		2.402	−1.690	⋯	⋯	133.7(5.16)	⋯
6254.258		2.277	−2.480	⋯	⋯	75.8(5.19)	⋯
6297.800		2.222	−2.74	⋯	55.7(6.76)	⋯	⋯
6318.018		2.452	−2.230	⋯	⋯	59.9(5.00)	⋯
6335.328		2.198	−2.230	⋯	⋯	79.7(4.81)	26.4(4.77)
6408.016		3.687	−1.048	59.4(5.56)	⋯	⋯	⋯
6421.349		2.278	−2.027	⋯	⋯	91.4(4.88)	22.2(4.58)
6430.85		2.18	−2.010	⋯	⋯	⋯	26.5(4.52)
4491.405	Fe II	2.855	−2.700	57.6(5.68)	⋯	⋯	⋯
4508.288		2.855	−2.210	67.8(5.39)	⋯	⋯	29.2(4.63)
4515.339		2.84	−2.480	62.5(5.53)	70.5(6.75)	22.9(5.11)	20.0(4.68)
4520.224		2.81	−2.600	55.1(5.47)	⋯	⋯	⋯
4629.339		2.807	−2.280	⋯	77.8(6.74)	⋯	⋯
4923.927		2.891	−1.260	⋯	⋯	80.7(4.93)	⋯
5197.56		3.23	−2.250	⋯	72.2(6.74)	⋯	⋯

Note. The numbers in the parenthesis in columns 5–8 give the derived absolute abundances from the respective lines.

(This table is available in its entirety in machine-readable form.)

Table A2
Equivalent Widths (in mÅ) of Lines Used for Deriving Elemental Abundances

Wavelength (Å)	El.	E_{low} (eV)	log *gf*	HE 0457−1805	HE 0920−0506	HE 1241−0337	HE 1327−2116
5682.633	Na I	2.102	−0.700	140.1(6.49)	66.9(5.89)	⋯	⋯
5688.205		2.1	−0.450	149.6(6.39)	⋯	⋯	17.1(4.28)
6154.226		2.102	−1.560	⋯	24.9(5.88)	42.1(5.48)	⋯
6160.747		2.104	−1.260	112.3(6.51)	46.1(6.04)	45.2(5.23)	⋯
4702.991	Mg I	4.346	−0.666	144.4(6.85)	173.0(7.54)	⋯	⋯
5528.405		4.346	−0.620	⋯	165.6(7.47)	81.6(5.08)	65.0(5.22)
5711.088		4.346	−1.833	106.2(7.04)	86.1(7.49)	16.5(5.26)	⋯
5690.425	Si I	4.929	−1.870	⋯	32.5(7.02)	9.2(5.75)	⋯
5772.148		5.080	−1.750	⋯	32.5(7.02)	10.7(5.87)	⋯
5948.541		5.083	−1.23	⋯	65.8(7.26)	⋯	⋯
6145.016		5.616	−0.820	24.6(6.10)	⋯	⋯	⋯
6237.319		5.613	−0.530	27.5(5.87)	⋯	⋯	10.2(5.45)

Note. The numbers in the parenthesis in columns 5–8 give the derived absolute abundances from the respective lines. Table A2 is published in its entirety in the machine-readable format. A portion is shown here for guidance regarding its form and content.

(This table is available in machine-readable form.)

Table A3
Lines Used to Derive the Elemental Abundance from Spectral Synthesis

Wavelength (Å)	El.	E_{low} (eV)	log *gf*	HE 0457−1805	HE 0920−0506	HE 1241−0337	HE 1327−2116
4320.730	Sc II	0.600	−1.950	⋯	⋯	0.91	⋯
4374.457		0.620	−0.440	⋯	⋯	⋯	0.04
4415.560		0.590	−1.700	⋯	⋯	1.09	⋯
5031.021		1.357	−0.260	⋯	⋯	⋯	0.02
6245.637		1.507	−0.980	1.85	2.14	⋯	-
6604.600		1.357	−1.480	⋯	2.14	⋯	⋯
4864.731	V I	0.017	−0.960	2.73	⋯	⋯	⋯
5727.048		1.080	−0.914	2.73	2.87	⋯	⋯
4451.586	Mn I	2.889	0.278	⋯	⋯	⋯	3.63
4470.140		2.941	−0.444	⋯	⋯	⋯	3.59
5516.774		2.178	−1.847	⋯	⋯	3.55	⋯
6013.513		3.072	−0.251	4.43	4.43	⋯	⋯
6021.819		3.075	0.0340	4.43	4.45	⋯	⋯
4118.770	Co I	1.050	−0.490	⋯	⋯	⋯	3.59
4121.320		0.920	−0.320	⋯	⋯	⋯	3.63
5342.695		4.021	0.690	3.58	⋯	⋯	⋯
5483.344		1.711	−1.490	⋯	4.19	⋯	⋯
5105.537	Cu I	1.389	−1.516	2.21	3.19	⋯	⋯
7800.259	Rb I	0.000	0.140	1.95	1.70	⋯	⋯
4607.327	Sr I	0.000	0.283	2.54	3.57	1.54	⋯
6435.004	Y I	0.066	−0.820	3.01	2.32	⋯	⋯
6134.585	Zr I	0.000	−1.280	3.03	3.05	1.44	1.81
5853.668	Ba II	0.295	−0.840	2.73	2.83	0.75	1.08
6496.897		0.604	−1.886	⋯	2.83	⋯	⋯
4748.726	La II	0.926	−0.540	1.37	1.60	⋯	⋯
4921.776		0.244	−0.450	1.40	1.60	−0.35	⋯
5259.379		0.173	−1.950	1.40	⋯	⋯	⋯
5303.528		0.321	−2.246	⋯	⋯	⋯	0.00
4129.725	Eu II	0.000	−1.294	⋯	−0.43	⋯	⋯
6437.640		1.319	−1.998	⋯	⋯	−1.58	⋯
6645.064		1.379	−0.517	−0.20	−0.39	−1.28	−1.16

Note. The numbers in columns 5–8 give the derived absolute abundances from the respective lines.

(This table is available in machine-readable form.)

ORCID iDs

J. Shejeelammal https://orcid.org/0000-0002-6234-4226
Aruna Goswami https://orcid.org/0000-0002-8841-8641

References

Abate, C., Stancliffe, R. J., & Liu, Z.-W. 2016, A&A, 587, A50
Abia, C., Busso, M., Gallino, R., et al. 2001, ApJ, 559, 1117
Allen, D. M., & Barbuy, B. 2006, A&A, 454, 895
Allen, D. M., Ryan, S. G., Rossi, S., Beers, T. C., & Tsangarides, S. A. 2012, A&A, 548, A34
Alonso, A., Arribas, S., & Martínez-Roger, C. 1999, A&AS, 140, 261
Alonso, A., Arribas, S., & Martínez-Roger, C. 2001, A&A, 376, 1039
Andrievsky, S. M., Spite, M., Korotin, S. A., et al. 2007, A&A, 464, 1081
Andrievsky, S. M., Spite, M., Korotin, S. A., et al. 2009, A&A, 494, 1083
Aoki, W., Ryan, S. G., Norris, J. E., et al. 2002, ApJ, 580, 1149
Aoki, W., Honda, S., Beers, T. C, et al. 2005, ApJ, 632, 611
Aoki, W., Frebel, A., Christlieb, N., et al. 2006, ApJ, 639, 897
Aoki, W., Beers, T. C., Christlieb, N., et al. 2007, ApJ, 655, 492
Aoki, W., Beers, T. C., Sivarani, T., et al. 2008, ApJ, 678, 1351
Arcones, A., & Thielemann, F. K. 2013, JPhG, 40, 013201
Arentsen, A., Starkenburg, E., Shetrone, M. D., et al. 2019, A&A, 621, A108
Asplund, M., Grevesse, N., Sauval, A. J., & Scott, P. 2009, ARA&A, 47, 481
Banerjee, P., Qian, Y.-Z., & Heger, A. 2018, ApJ, 865, 120
Beers, T. C. 1999, in ASP Conf. Ser., 165, The Third Stromlo Symposium: The Galactic Halo, ed. B. K. Gibson, R. S. Axelrod, & M. E. Putman (San Francisco, CA: ASP), 202
Beers, T. C., & Christlieb, N. 2005, ARA&A, 43, 531
Beers, T. C., Placco, V. M., Carollo, D., et al. 2017, ApJ, 835, 81
Bergemann, M., Hansen, C. J., Bautista, M., & Ruchti, G. 2012, A&A, 546, A90
Bessell, M. S., Collet, R., Keller, S. C., et al. 2015, ApJL, 806, L16
Bisterzo, S., Gallino, R., Straniero, O., Cristallo, S., & Käppeler, F. 2010, MNRAS, 404, 1529
Bisterzo, S., Gallino, R., Straniero, O., Cristallo, S., & Käppeler, F. 2011, MNRAS, 418, 284
Bonifacio, P., Caffau, E., Spite, M., et al. 2015, A&A, 579, A28
Busso, M., Gallino, R., Lambert, D. L., Travaglio, C., & Smith, V. V. 2001, ApJ, 557, 802
Campbell, S. W., & Lattanzio, J. C. 2008, A&A, 490, 769
Campbell, S. W., Lugaro, M., & Karakas, A. I. 2010, A&A, 522, L6
Castelli, F., & Kurucz, R. L. 2003, in Proc. of the IAU Symp. No 210 Vol. 210, Modelling of Stellar Atmospheres, ed. N. Piskunov, W. Weiss, & D. Gray (San Francisco, CA: ASP), A20
Cayrel, R., Depagne, E., Spite, M., et al. 2004, A&A, 416, 1117
Charbonnel, C. 1995, ApJL, 453, L41
Charbonnel, C., Brown, J. A., & Wallerstein, G. 1998, A&A, 332, 204
Chiappini, C. 2013, AN, 334, 595
Choplin, A., Hirschi, R., Meynet, G., & Ekström, S. 2017, A&A, 607, L3
Christlieb, N. 2003, RvMA, 16, 191
Christlieb, N., Green, P. J., Wisotzki, L., & Reimers, D. 2001, A&A, 375, 366
Cowan, J. J., & Rose, W. K. 1977, ApJ, 212, 149
Cristallo, S., Straniero, O., Gallino, R., et al. 2009, ApJ, 696, 797
Cristallo, S., Piersanti, L., Straniero, O., et al. 2011, ApJS, 197, 17
Cristallo, S., Straniero, O., Piersanti, L., & Gobrecht, D. 2015, ApJS, 219, 40
de Castro, D. B., Pereira, C. B., Roig, F., et al. 2016, MNRAS, 459, 4299
Denissenkov, P. A., Herwig, F., Battino, U., et al. 2017, ApJL, 834, L10
Doherty, C. L., Gil-Pons, P., Siess, L., Lattanzio, J. C., & Lau, H. H. B. 2015, MNRAS, 446, 2599
Drout, M. R., Piro, A. L., Shappee, B. J., et al. 2017, Sci, 358, 1570
Frebel, A., Christlieb, N., Norris, J. E., et al. 2006, ApJ, 652, 1585
Frebel, A., Collet, R., Eriksson, K., Christlieb, N., & Aoki, W. 2008, ApJ, 684, 588
Fujimoto, M. Y., Iben Icko, J., & Hollowell, D. 1990, ApJ, 349, 580
Fujimoto, M. Y., Ikeda, Y., & Iben Icko, J. 2000, ApJL, 529, L25
Gaia Collaboration, Katz, D., Antoja, T., et al. 2018, A&A, 616, A11
Gallino, R., Bisterzo, S., Husti, L., et al. 2006, in Int. Symp. on Nuclear Astrophysics—Nuclei in the Cosmos, ed. A. Mengoni, J. Cederkall, J. D'Auria et al. (Trieste: PoS), 100.1
Girardi, L., Bressan, A., Bertelli, G., & Chiosi, C. 2000, A&AS, 141, 371
Goriely, S., & Mowlavi, N. 2000, A&A, 362, 599
Goriely, S., & Siess, L. 2005, in Proc. Int. Astronomical Union 228, From Lithium to Uranium: Elemental Tracers of Early Cosmic Evolution, ed. V. Hill, P. Francois, & F. Primas (Cambridge: Cambridge Univ. Press), 451
Goswami, A. 2005, MNRAS, 359, 531
Goswami, A., Aoki, W., & Karinkuzhi, D. 2016, MNRAS, 455, 402
Goswami, P. P., Rathour, R. S., & Goswami, A. 2021, A&A, 649, A49
Gratton, R. G., Sneden, C., Carretta, E., & Bragaglia, A. 2000, A&A, 354, 169
Hampel, M., Stancliffe, R. J., Lugaro, M., & Meyer, B. S. 2016, ApJ, 831, 171
Hampel, M., Karakas, A. I., Stancliffe, R. J., Meyer, B. S., & Lugaro, M. 2019, ApJ, 887, 11
Hansen, T., Hansen, C. J., Christlieb, N., et al. 2015, ApJ, 807, 173
Hansen, T. T., Andersen, J., Nordström, B., et al. 2016a, A&A, 586, A160
Hansen, T. T., Andersen, J., Nordström, B., et al. 2016b, A&A, 588, A3
Hansen, C. J., Nordström, B., Hansen, T. T., et al. 2016c, A&A, 588, A37
Hansen, C. J., Hansen, T. T., Koch, A., et al. 2019, A&A, 623, A128
Hartwig, T., Yoshida, N., Magg, M., et al. 2018, MNRAS, 478, 1795
Heger, A., & Woosley, S. E. 2010, ApJ, 724, 341
Hollowell, D., Iben Icko, J., & Fujimoto, M. Y. 1990, ApJ, 351, 245
Honda, S., Aoki, W., Kajino, T., et al. 2004, ApJ, 607, 474
Husti, L., Gallino, R., Bisterzo, S., Straniero, O., & Cristallo, S. 2009, PASA, 26, 176
Jacobson, H. R., Pilachowski, C. A., & Friel, E. D. 2005, AAS Meeting, 207, 71.16
Johnson, J. A., Herwig, F., Beers, T. C., & Christlieb, N. 2007, ApJ, 658, 1203
Jones, S., Ritter, C., Herwig, F., et al. 2016, MNRAS, 455, 3848
Jonsell, K., Barklem, P. S., Gustafsson, B., et al. 2006, A&A, 451, 651
Jorissen, A., Van Eck, S., Mayor, M., & Udry, S. 1998, A&A, 332, 877
Jorissen, A., Van Eck, S., Van Winckel, H., et al. 2016a, A&A, 586, A158
Jorissen, A., Hansen, T., Van Eck, S., et al. 2016b, A&A, 586, A159
Käppeler, F., Gallino, R., Bisterzo, S., & Aoki, W. 2011, RvMP, 83, 157
Karakas, A. I. 2010, MNRAS, 403, 1413
Karakas, A. I., & Lattanzio, J. C. 2003, PASA, 20, 279
Karakas, A. I., & Lattanzio, J. C. 2014, PASA, 31, e030
Karakas, A. I., García-Hernández, D. A., & Lugaro, M. 2012, ApJ, 751, 8
Karinkuzhi, D., & Goswami, A. 2014, MNRAS, 440, 1095
Karinkuzhi, D., & Goswami, A. 2015, MNRAS, 446, 2348
Karinkuzhi, D., Van Eck, S., Jorissen, A., et al. 2018, A&A, 618, A32
Karinkuzhi, D., Van Eck, S., Goriely, S., et al. 2021, A&A, 645, A61
Kennedy, C. R., Sivarani, T., Beers, T. C., et al. 2011, AJ, 141, 102
Kobayashi, C., Karakas, A. I., & Umeda, H. 2011, MNRAS, 414, 3231
Kobayashi, C., Karakas, A. I., & Lugaro, M. 2020, ApJ, 900, 179
Koch, A., Reichert, M., Hansen, C. J., et al. 2019, A&A, 622, A159
Kordopatis, G., Gilmore, G., Steinmetz, M., et al. 2013, AJ, 146, 134
Lambert, D. L., & Luck, R. E. 1976, Obs, 96, 100
Lau, H. H. B., Stancliffe, R. J., & Tout, C. A. 2009, MNRAS, 396, 1046
Lind, K., Asplund, M., Barklem, P. S., & Belyaev, A. K. 2011, A&A, 528, A103
Lippuner, J., Fernández, R., Roberts, L. F., et al. 2017, MNRAS, 472, 904
Lucatello, S., Tsangarides, S., Beers, T. C., et al. 2005, ApJ, 625, 825
Luck, R. E. 2017, AJ, 153, 21
Luck, R. E., & Heiter, U. 2007, AJ, 133, 2464
Lugaro, M., Campbell, S. W., & de Mink, S. E. 2009, PASA, 26, 322
Marigo, P. 2002, A&A, 387, 507
Mashonkina, L., Zhao, G., Gehren, T., et al. 2008, A&A, 478, 529
Masseron, T., Johnson, J. A., Plez, B., et al. 2010, A&A, 509, A93
McSaveney, J. A., Wood, P. R., Scholz, M., Lattanzio, J. C., & Hinkle, K. H. 2007, MNRAS, 378, 1089
Mowlavi, N. 1999, A&A, 350, 73
Nomoto, K., Kobayashi, C., & Tominaga, N. 2013, ARA&A, 51, 457
Placco, V. M., Frebel, A., Beers, T. C., & Stancliffe, R. J. 2014, ApJ, 797, 21
Placco, V. M., Sneden, C., Roederer, I. U., et al. 2021, RNAAS, 5, 92
Purandardas, M., & Goswami, A. 2021, ApJ, 922, 28
Purandardas, M., Goswami, A., Goswami, P. P., Shejeelammal, J., & Masseron, T. 2019, MNRAS, 486, 3266
Raskin, G., van Winckel, H., Hensberge, H., et al. 2011, A&A, 526, A69
Reddy, B. E., Lambert, D. L., & Allende Prieto, C. 2006, MNRAS, 367, 1329
Romano, D., Karakas, A. I., Tosi, M., & Matteucci, F. 2010, A&A, 522, A32
Rosswog, S., Korobkin, O., Arcones, A., Thielemann, F. K., & Piran, T. 2014, MNRAS, 439, 744
Shejeelammal, J., & Goswami, A. 2021, ApJ, 921, 77
Shejeelammal, J., Goswami, A., Goswami, P. P., Rathour, R. S., & Masseron, T. 2020, MNRAS, 492, 3708
Shejeelammal, J., Goswami, A., & Shi, J. 2021, MNRAS, 502, 1008
Shetrone, M. D. 2003, ApJL, 585, L45
Sloan, G. C., Kraemer, K. E., Wood, P. R., et al. 2008, ApJ, 686, 1056
Sneden, C. A. 1973, PhD thesis, Univ. Texas at Austin
Sneden, C., Cowan, J. J., & Gallino, R. 2008, ARA&A, 46, 241
Spite, M., Cayrel, R., Plez, B., et al. 2005, A&A, 430, 655
Spite, M., Cayrel, R., Hill, V., et al. 2006, A&A, 455, 291
Spite, M., Caffau, E., Bonifacio, P., et al. 2013, A&A, 552, A107

Stancliffe, R. J., Dearborn, D. S. P., Lattanzio, J. C., Heap, S. A., & Campbell, S. W. 2011, ApJ, 742, 121
Starkenburg, E., Shetrone, M. D., McConnachie, A. W., & Venn, K. A. 2014, MNRAS, 441, 1217
Surman, R., McLaughlin, G. C., Ruffert, M., Janka, H. T., & Hix, W. R. 2008, ApJL, 679, L117
Takeda, Y., Zhao, G., Takada-Hidai, M., et al. 2003, ChJAA, 3, 316
Tominaga, N., Iwamoto, N., & Nomoto, K. 2014, ApJ, 785, 98
Travaglio, C., Gallino, R., Busso, M., & Gratton, R. 2001, ApJ, 549, 346
Travaglio, C., Gallino, R., Arnone, E., et al. 2004, ApJ, 601, 864
van Raai, M. A., Lugaro, M., Karakas, A. I., García-Hernández, D. A., & Yong, D. 2012, A&A, 540, A44
Vanture, A. D. 1992, AJ, 104, 1997
Venn, K. A., Irwin, M., Shetrone, M. D., et al. 2004, AJ, 128, 1177
Yang, G.-C., Liang, Y.-C., Spite, M., et al. 2016, RAA, 16, 19
Yoon, J., Beers, T. C., Placco, V. M., et al. 2016, ApJ, 833, 20